

The nature of dynamic local order in $\text{CH}_3\text{NH}_3\text{PbI}_3$ and $\text{CH}_3\text{NH}_3\text{PbBr}_3$

Nicholas J Weadock^{1,2*†}, Tyler C Sterling^{3†}, Julian A
Vigil^{4,5}, Aryeh Gold-Parker⁵, Ian C Smith⁵, Ballal
Ahammed⁶, Matthew J Krogstad⁷, Feng Ye⁸, David
Voneshen^{9,10}, Peter M Gehring, Hans-Georg Steinrück¹², Elif
Ertekin⁶, Hemamala I Karunadasa^{5,13}, Dmitry Reznik^{3*}
and Michael F Toney^{1,2,14*}

¹Materials Science and Engineering, University of Colorado,
Boulder, Boulder, CO, 80309, USA.

²Department of Chemical and Biological Engineering, University
of Colorado, Boulder, Boulder, CO, 80309, USA.

³Department of Physics, University of Colorado, Boulder,
Boulder, CO, 80309, USA.

⁴Department of Chemical Engineering, Stanford University,
Stanford, CA, 94305, USA.

⁵Department of Chemistry, Stanford University, Stanford, CA,
94305, USA.

⁶Department of Mechanical Science & Engineering and Materials
Research Laboratory, University of Illinois at
Urbana-Champaign, Urbana, IL, 61801, USA.

⁷Advanced Photon Source, Argonne National Lab, Lemont, IL,
60439, USA.

⁸Neutron Scattering Division, Oak Ridge National Laboratory,
Oak Ridge, TN, 37830, USA.

⁹ISIS Facility, Rutherford Appleton Laboratory, Chilton, Didcot,
Oxon OX11 0QX, United Kingdom.

¹⁰Department of Physics, Royal Holloway University of London,
Egham TW20 0EX, United Kingdom.

¹¹NIST Center for Neutron Research, National Institute of
Standards and Technology, Gaithersburg, MD, 20899, USA.

¹²Department Chemie, Universität Paderborn, Paderborn, Germany.

¹³Stanford Institute for Materials and Energy Sciences, SLAC National Accelerator Laboratory, Menlo Park, CA, 94025, USA.

¹⁴Renewable and Sustainable Energy Institute (RASEI), University of Colorado, Boulder, CO, 80303, USA.

*Corresponding author(s). E-mail(s):
nicholas.weadock@colorado.edu; dmitry.reznik@colorado.edu;
michael.toney@colorado.edu;

†These authors contributed equally to this work.

Abstract

Hybrid lead halide perovskites (LHPs) are a class of semiconductor with novel properties that are distinctively governed by structural fluctuations. Diffraction experiments sensitive to average, long-range order reveal a cubic structure in the device-relevant, high-temperature phase. Local probes find additional short-range order with lower symmetry that may govern the structure-function relationships of LHPs. However, the dimensionality, participating atoms, and dynamics of this short-range order are unresolved, impeding our understanding of technologically relevant properties including long carrier lifetimes and facile halide migration. Here, we determine the true structure of two prototypical hybrid LHPs, $\text{CH}_3\text{NH}_3\text{PbI}_3$ and $\text{CH}_3\text{NH}_3\text{PbBr}_3$, using a combination of single-crystal X-ray and neutron diffuse scattering, neutron inelastic spectroscopy, and molecular dynamics simulations. The remarkable collective dynamics we found are not suggested by previous studies and consist of a network of local two-dimensional, circular pancake-like regions of dynamically tilting lead halide octahedra (lower symmetry) that induce longer range intermolecular correlations within the CH_3NH_3^+ sublattice. The dynamic local structure can introduce transient ferroelectric or antiferroelectric domains that increase charge carrier lifetimes, and strongly affect the halide migration, a poorly understood degradation mechanism. Our approach of co-analyzing single-crystal X-ray and neutron diffuse scattering data with MD simulations will provide unparalleled insights into the structure of hybrid materials and materials with engineered disorder.

Keywords: Metal halide perovskites, Diffuse scattering, Local structure, Ion migration

The crystal structure and associated symmetry of a material are key determinants of mechanical, electronic, optical, and thermal properties. One has to

look no further than seminal condensed matter physics textbooks for derivations of these properties made possible by consideration of the long-range or average order determined by the crystal lattice and translational symmetry [1, 2]. However, in many materials including disordered rocksalts and intercalation compounds used for battery cathodes, relaxor ferroelectrics, thermoelectrics, and oxide and halide perovskites, the important properties are not well described by the long-range structure. Instead it is short-range order that dominates aspects of the structure-function relationship [3–9]. In scattering experiments, short-range or local order manifests as diffuse scattering; a result of static and dynamic deviations from the average structure. Fixed chemical or local structural correlations result in static diffuse scattering, whereas thermal diffuse scattering arises from dynamic displacements due to lattice dynamics [10]. Resolving structural correlations in disordered materials has recently become more feasible with the development of high flux, single crystal X-ray and neutron diffuse scattering instruments and sophisticated modeling algorithms [4, 11–15], opening up enormous opportunities to understand how local order impacts materials properties.

Organic-inorganic metal halide perovskites are a recently re-invigorated class of semiconductors with remarkable optoelectronic performance that defies traditional intuition: Lead-based metal halide perovskites (LHPs) possess a mechanically soft, defect-tolerant crystal lattice with strong structural disorder and mobile ions at modest temperatures [16]. Fluctuations in the orbital overlaps arising from large thermal displacements of iodide in methylammonium (CH_3NH_3^+ , $\text{CD}_3\text{ND}_3^+ = \text{MA}$) lead iodide directly influence the temperature dependence of the electron (or hole) mobility and optical bandgap [17]. X-ray and neutron diffraction measurements, which probe long-range order, report that the high-temperature phase is cubic with well-defined Bragg peaks [18–20]. This cubic perovskite structure is shown in Figure 1a and consists of corner-sharing PbX_6 ($\text{X} = \text{I}^-, \text{Br}^-$) octahedra surrounding a dynamically disordered MA^+ cation within the cuboctahedral interstice. Measurements probing short-range order in the high-temperature phase, however, suggest the local structure is of lower symmetry [21–25]. The lack of consensus regarding the exact symmetry and dynamics of this enigmatic local structure limits our understanding and control of optoelectronic properties and ion migration in LHPs. Short-range order arising from dynamic two-dimensional correlations of lead bromide octahedra has recently been identified in CsPbBr_3 [9]. These correlations are most prominent in the cubic phase above 433 K and may not play a significant role in CsPbBr_3 -based device operation. The significance and prevalence of such correlations in hybrid LHPs, including contributions from the organic cations, is not resolved.

Ion migration in LHPs, especially under illumination, is detrimental to device performance and stability yet the origin is not well understood. Consequences of ion migration include formation of space charge potentials at interfaces, accelerated degradation and loss of constituent elements, and light-induced phase segregation in mixed-halide compositions [26]. A complete

picture of the high-temperature structure and dynamics is essential to model ion migration pathways accurately [27]. It is also important to characterize the short-range order on the organic sublattice, as the rotating MA^+ molecular dipoles may screen band-edge charge carriers and extend carrier lifetimes [28].

We use single crystal X-ray and neutron diffuse scattering and neutron spectroscopy, combined with molecular dynamics (MD) simulations, to uncover the true structure and dynamics of the nominally simple cubic ($Pm\bar{3}m$) phases of MAPbI_3 (> 327 K) and MAPbBr_3 (> 237 K). We find that the cubic phase (Fig. 1a, c) is comprised of dynamic, two-dimensional roughly circular “pancakes” of tilted lead halide octahedra which align along any of the three principal axes of the cubic structure and (Fig. 1b, d) induce additional structural correlations of the organic sublattice in the layers sandwiching the octahedra. Taken together, these regions of dynamic local order are several unit cells in diameter with lifetimes on the order of several picoseconds, resulting in a dynamic landscape for charge carriers and ion migration. This extended dynamic local order was neither observed nor predicted in previous studies of structural dynamics in hybrid LHPs [29–32]. Embedded within this dynamic structure we find additional static 3D droplets of the intermediate tetragonal phase, consistent with previous reports [22, 25]. The structural correlations on the MA^+ sublattice are a unique characteristic in these hybrid systems with implications discussed below.

The experimental scattering function $S(\mathbf{Q})$ from the cubic phase of MAPbI_3 at 345 K is shown in Fig. 2. Specifically, we present the $L = 0.5, 1.5$ planes measured with both X-ray (XDS, Fig. 2a,c, left panels) and neutron diffuse scattering (NDS, Fig 2b,d, left panels). $S(\mathbf{Q})$ calculated from atomic trajectories obtained with MD simulations of MAPbI_3 , see Methods, is plotted in the right-hand panels of a-d and both panels of g,h for comparison.

The experimental $S(\mathbf{Q})$ of the cubic phase of MAPbBr_3 at 250 K is plotted in Fig. S1 and show diffuse scattering intensity profiles for XDS and NDS that are nearly identical to MAPbI_3 .

Our approach to solving the true structure of the nominally simple cubic MAPbI_3 and MAPbBr_3 involves decomposing the observed diffuse scattering profile into four components and analyzing their energy and \mathbf{Q} -dependence. These components include: (1) rods of constant (XDS) or varied (NDS) intensity spanning the BZ edge (M-R direction in Fig. 1, $q = [0.5, 0.5, L]$); (2) an additional contribution centered at the R-point [$q = (0.5, 0.5, 0.5)$]; (3) broad intensity centered at the X-point [$q = (0.5, 0, 0)$] observed previously and discussed in the SI; and (4) contributions from the MA^+ sublattice deduced from the alternating diffuse rod intensity profile observed in NDS but not XDS. This difference between XDS and NDS is highlighted with one-dimensional line cuts of XDS and NDS data shown in Figs. 2e and f. Specifically, the peaks at $K = \pm 2.5$ originating from the extended rod along H in XDS are not observed in the NDS data. Our analysis is complemented by MD simulations of MAPbI_3 which reproduce the experimental diffuse scattering. The experimental and calculated XDS (Fig. 2) show remarkable agreement. Comparing

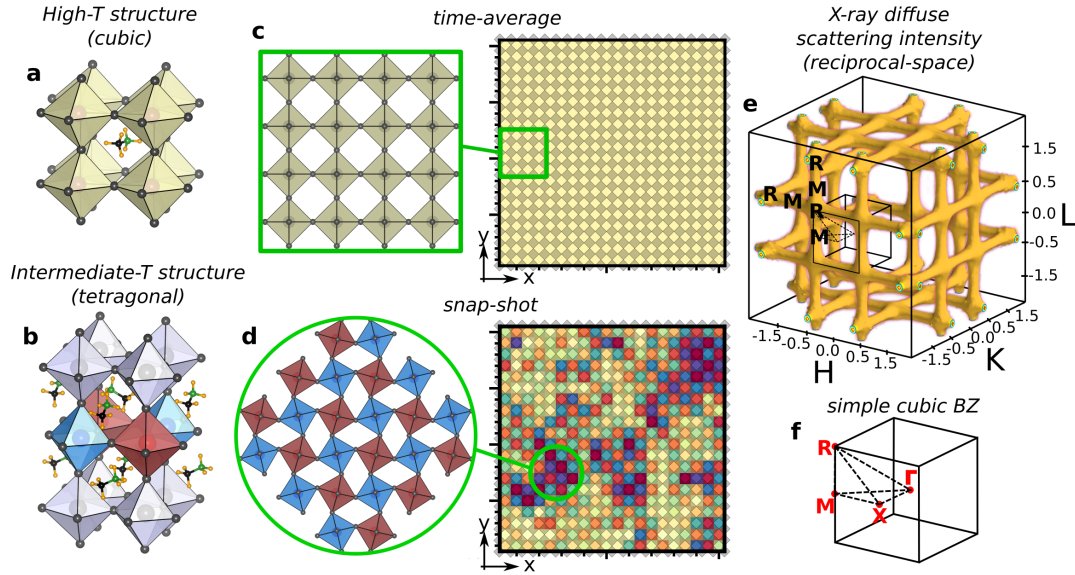


Fig. 1 a, c Visualizations of the high-temperature cubic structure and b, the intermediate-temperature tetragonal structure of MAPbI_3 and MAPbBr_3 . MA^+ disorder has been omitted for clarity. The cubic-tetragonal transition in MAPbI_3 and MAPbBr_3 occurs at 328 and 236 K, respectively, by the freezing out of octahedral tilts in an out-of-phase pattern [18, 33]. d, Instantaneous snapshots of the cubic structure from MD reveal dynamic two-dimensional correlations consisting of tilted PbX_6 octahedra that can orient to be perpendicular to any of the three principal axes. e, 3D visualization of the X-ray diffuse scattering intensity generated by the structural correlations. The diffuse volume is indexed by Miller indices H,K,L, of which integer values enumerate each Brillouin Zone (BZ). f, The simple cubic BZ with high symmetry points indicated in red. The diffuse rods in e run along the BZ edge, connecting M and R points.

the two results in a root-mean-square error of 3.9% (see Figs. S2,3 and related discussion) after adjusting only the background and scaling of the calculated $S(\mathbf{Q})$. The agreement between the experimental and calculated NDS is very good, however there are small differences in intensities highlighted in Fig. S4 that likely arise from the classical potentials used here. Given the good agreement, we examine the real-space structure simulated with MD to determine the origin of the diffuse scattering.

The XDS rods of diffuse scattering have constant intensity along the entire BZ edge (Fig. S5) and a width larger than the instrument resolution ($\approx 0.02\text{\AA}^{-1}$). This lineshape arises from two-dimensional structural correlations in real-space. We show these correlations in Fig. 3, which presents a simplified visualization of the MD simulation. These plots track PbI_6 octahedral rotations, defined by azimuthal rotation angle ϕ about the [001] (Fig. 3a,b) or [010] (Fig. 3c,d) directions. Correlated regions of alternating large tilts are identified by neighboring red and blue pixels (representing octahedra) in Fig. 3a and d. Along the axis of rotation indicated in the corresponding schematic the tilts are uncorrelated between planes (Fig. 3b,c), revealing the existence of two-dimensional pancakes of tilted octahedra with a diameter on the order of 5 unit cells. These regions are reminiscent of tilts associated with

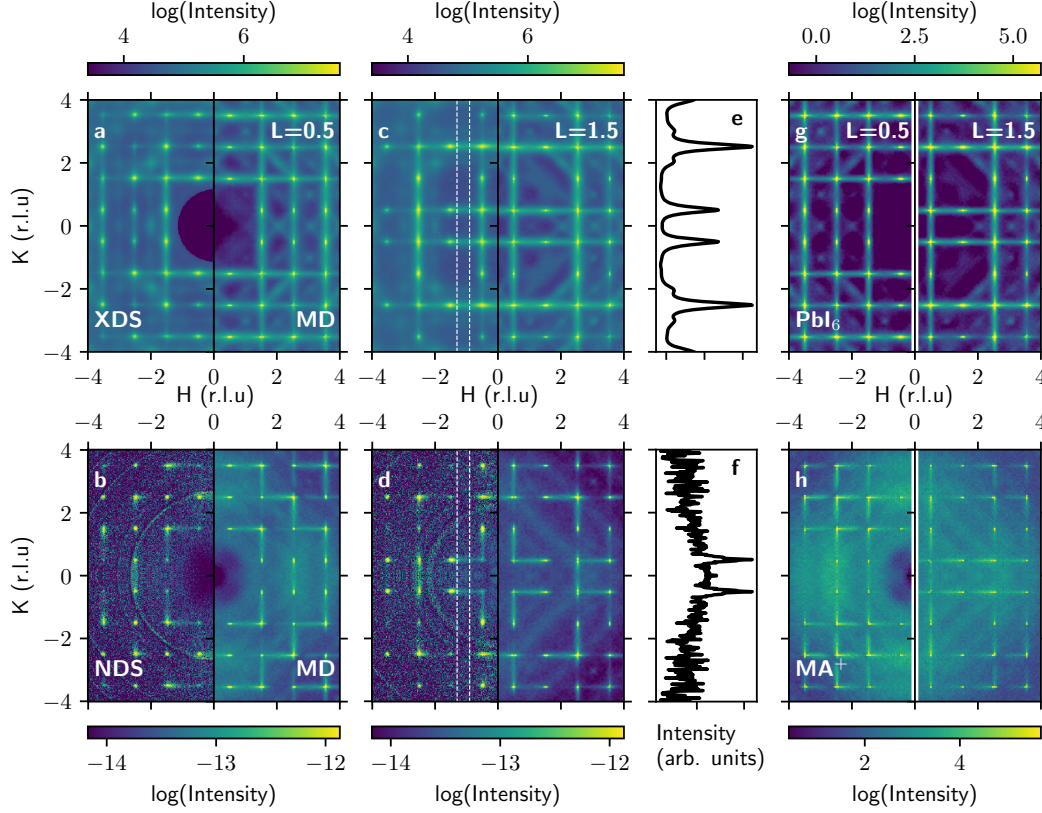


Fig. 2 Experimental $S(\mathbf{Q})$ for MAPbI₃ measured with XDS (a,c left panels) and NDS (b,d left panels) at 345 K. The XDS data are inherently energy integrated whereas the NDS data are static with a 0.9 meV FWHM energy bandwidth. Panels a,b correspond to the $L = 0.5$ plane, and panels c,d the $L = 1.5$ plane. No Bragg intensity is expected in these half-order planes; therefore any intensity is diffuse scattering. The faint circular rings in the experimental NDS data are residual Debye-Scherrer diffraction rings from the aluminum sample holder. Theoretical $S(\mathbf{Q})$, calculated from MD simulations (± 1 meV bandwidth), are plotted in the right panels of a-d. In a,c, X-ray form factors were used whereas b,d,g,h were calculated using neutron scattering lengths (see supplementary information [34]). e,f plot one-dimensional linecuts along K , integrating 0.7:H:1.3 and 1.4:L:1.6, which highlight the differences between XDS and NDS. Panels g,h plot the PbI₆ and MA⁺ contributions to the calculated neutron $S(\mathbf{Q})$, respectively, with the left panels corresponding to $L = 0.5$ and the right panels $L = 1.5$. We note that the NDS plotted here corresponds to the elastic scattering channel of the CORELLI spectrometer (~ 0.9 meV full width at half-maximum for $E_i = 30$ meV)[12].

the tetragonal structure in Fig. 1b. The tilts generate in-plane antiphase structural correlations with a periodicity of $2a$. The associated wave vector of the correlation is $q = 2\pi/2a = \pi/a$, which is the zone boundary for the simple cubic BZ. The tilted regions are confined to a single PbI₆ sheet and therefore the diffuse scattering intensity manifests as rods.

The same structural correlations are present in the cubic phase of MAPbBr₃, since the XDS and NDS are qualitatively identical to that of MAPbI₃ (Fig. S1, 2). Extended diffuse rods observed in the all-inorganic CsPbBr₃ [9] point to the existence of two-dimensional structural correlations of lead halide octahedra in all LHPs with a high temperature cubic structure.

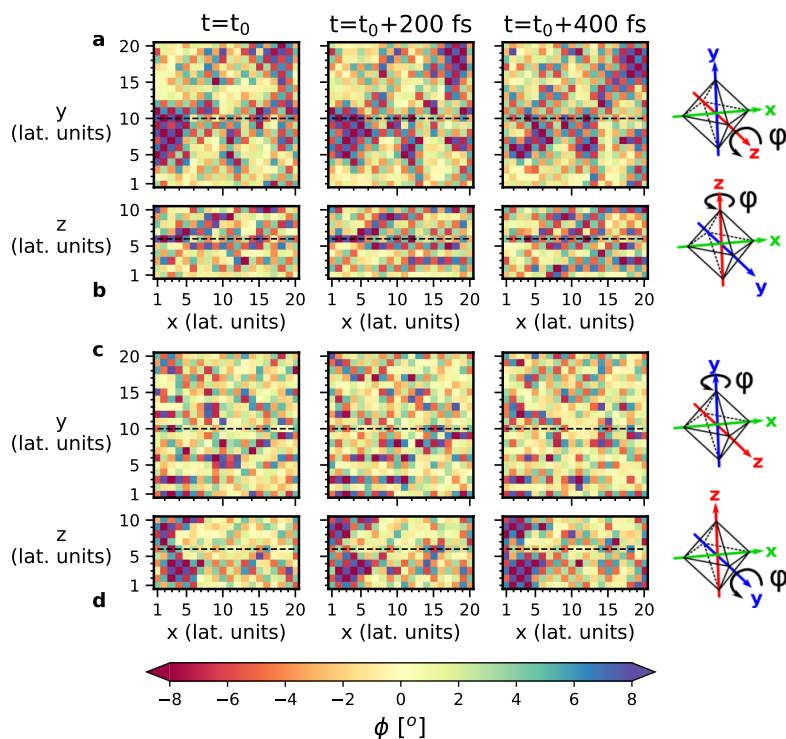


Fig. 3 Spatiotemporal dynamics of PbI_6 octahedral rotations in cubic MAPbI_3 calculated from MD. Each pixel encodes the octahedral rotation angle ϕ about the z -axis [a and b] and the y -axis [c and d]. The columns are offset in time by $\Delta t=200$ fs to highlight the dynamic nature. The top rows [a and c] are in the x - y plane and the bottom rows [b and d] are in the x - z plane. In a and d, the rotation is about the axis perpendicular to the plane as shown by the diagrams on the right. In b and c, the rotation is about an axis parallel to the figure's vertical axis. The dashed lines indicate the intersection between the x - y plane in a and c and the x - z plane in b and d. Note that the two-dimensional regions visible in a, d are one unit cell thick in the normal direction b, c.

Intermolecular structural correlations in the MA^+ sublattice are implied from the alternating intensity pattern of the diffuse rods present in NDS but not XDS. The MA^+ correlations are explored in the calculated $S(\mathbf{Q})$ in Figs. 2g,h, and S6-8. Specifically, we set the neutron scattering lengths of Pb and I to zero in the calculation to isolate the contribution from the MA^+ cation (Figs. 2h, S6c, g, k and S7), and C, N, and D to zero to isolate contributions from the inorganic octahedra (Figs. 2g, S6b, f, j and S7). Diffuse scattering from the inorganic framework manifests as extended diffuse rods along the zone edge, resembling the experimental XDS as the X-ray atomic form factors for C, N, D are small compared to those for Pb and I and contribute little intensity. The calculated $S(\mathbf{Q})$ from CD_3ND_3^+ shows remarkable behavior (Figs. 2h, S6, S7), namely well-defined diffuse rods along the zone edges in addition to broad, isotropic intensity. This broad, isotropic component is a result of uncorrelated MA^+ dynamics [31, 32] commonly associated with the nominally cubic phases of LHPs. The presence of additional zone edge intensity, however, shows that previously unreported intermolecular structural correlations exist on the MA^+ sublattice. These local correlations are not purely 2D as the intensity

varies along individual diffuse rods in the MA^+ $S(\mathbf{Q})$ (Fig. S6,7). Layers of PbX_6 octahedra are sandwiched between layers of MA^+ cations, therefore we expect the out-of-plane MA^+ structural correlations to extend at least two unit cells. Finally, the MA^+ and PbX_6 correlations are connected as evidenced by a nonzero interference term, shown in Fig. S8, which results in the alternating diffuse intensity profile observed in NDS.

We propose that MA^+ orientation is driven by PbX_6 tilts; the MA^+ molecules orient to favor the lowest energy configuration defined by the distorted cuboctahedral geometry of the tilted regions and electrostatic interactions between lead halide octahedra and polar MA^+ molecules [35, 36]. The existence of 2D correlations on the PbBr_6 sublattice in CsPbBr_3 supports this prediction as the Cs^+ cations are not expected to influence the PbBr_6 octahedra through hydrogen bonding. [9].

The lateral size of 2D pancakes, given by the correlation length, ξ , is obtained from the \mathbf{Q} -linewidth of the XDS and NDS diffuse rods. We fit the intensity of one-dimensional cuts in \AA^{-1} across various diffuse rods to a Lorentzian lineshape in accordance with Ornstein-Zernike theory for exponentially decaying spatial correlations:

$$S(\mathbf{q}) \propto \frac{\Gamma}{\Gamma^2 + (q - q_0)^2} \quad (1)$$

where $\Gamma = 1/\xi$ is the half-width at half-maximum (HWHM) of the fitted Lorentzian and ξ is the correlation length [6, 37]. Correlation lengths of 4-6 unit cells (~ 3 nm) in diameter are obtained for MAPbBr_3 and MAPbI_3 as reported in Table S1. Similar ξ are obtained from NDS and XDS, indicating the in-plane ξ of the 2D pancakes are nearly equivalent for the PbX_6 and MA^+ sublattices. We also calculate ξ directly from the MD simulations, see Figs. S9-12 and related discussion, and find values consistent with experiment.

Molecular dynamics simulations show that the 2D structural correlations are transient and diffusive, with dynamics of the octahedral correlations tracked in Fig. 3 and Supplementary Videos 1 and 2. We investigate the dynamics of the PbI_6 and MA^+ correlations by evaluating the energy dependence obtained from the dynamical structure factor $S(\mathbf{Q}, E = \hbar\omega)$ measured with neutron inelastic spectroscopy (INS) on MAPbI_3 at 340 K. The $S(\mathbf{Q}, E)$ in the $L = 0.5$ plane, integrated from $-1 \leq E \leq 1$ meV is shown in the right-hand panel of Fig. 4a and matches that observed with NDS (Fig. 2b) and that calculated from MD (left-hand panel of Fig. 4b). A slice of $S(\mathbf{Q}, E)$ along the diffuse rod presented in Fig. 4b shows that the intensity is centered at $E = 0$ meV with no inelastic component visible. Incoherent-background-subtracted energy scans (integrated along the length of the diffuse rod) show a finite, quasielastic component as exemplified in Fig. 4d. Quasielastic scattering is a result of diffusive or relaxational motions involving small energy transfers, manifesting as a peak centered at $E = 0$ meV with a non-zero linewidth. The scattering is fit to a relaxational (Lorentzian) model, broadened by the resolution function, as shown in Fig. 4d. The average energy HWHM, plotted in Fig. 4e, is

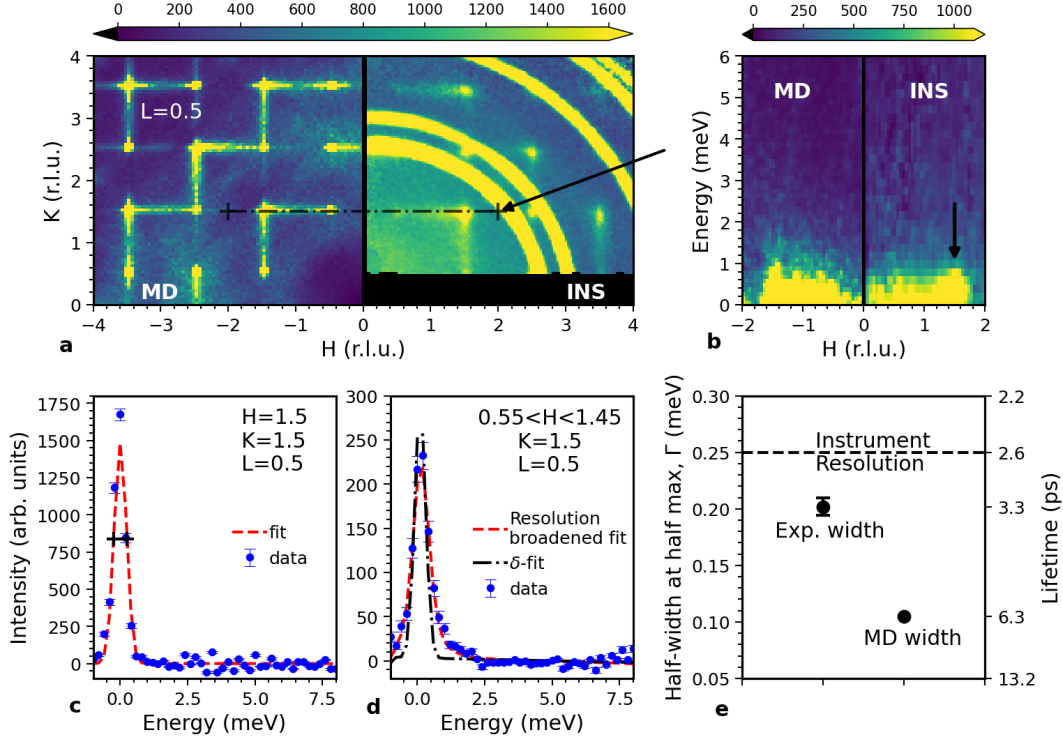


Fig. 4 Theoretical and experimental $S(\mathbf{Q}, E)$ of MAPbI_3 , highlighting the energy dependence of the diffuse scattering rods. Neutron inelastic scattering data (right panels of a,b; and c,d) were measured at 340 K. In a, the $S(\mathbf{Q})$ from MD and experiment is integrated from $-1 \leq E \leq 1\text{meV}$. Powder rings from the aluminum sample holder are visible in a. Constant- \mathbf{Q} scans at the R-point (c, integrated along 1.45:H:1.55, 1.45:K:1.55, 0.45:L:0.55) and along the diffuse rod (d, integrated along 0.55:H:1.45, 1.45:K:1.55, 0.45:L:0.55) are fit to Gaussian and resolution-broadened Lorentzian lineshapes with resolution linewidth of 0.5 meV FWHM, respectively (red dashed lines). The black line in c indicates the 0.5 meV resolution FWHM. In d, we include the resolution lineshape (black dash-dot line), demonstrating a finite width beyond the resolution. In e, the average HWHM (and corresponding lifetime) obtained from Lorentzian fits to constant- \mathbf{Q} scans are plotted for experiments and MD. The dashed line represents the energy resolution of the MERLIN spectrometer.

0.20 ± 0.01 meV with a corresponding lifetime $\tau = \hbar/\text{HWHM}$ of 3.25 ± 0.13 ps. Lifetimes are obtained in the same manner from the calculated $S(\mathbf{Q}, E)$ as shown in Fig. S13, and the average lifetime of 6.3 ps is reported in Fig. 4e. We note that these lifetimes are consistent with the mean residence time for rotations of the C-N bond in cubic MAPbI_3 , suggesting that MA^+ reorientations are in part driven by the PbX_6 correlations [32]. Overall, the structural correlations are dynamic with finite lifetime of several picoseconds.

R-point scattering ($\mathbf{Q} = [1.5, 1.5, 0.5]$, Fig. 4c) noted above has been investigated previously and is attributed to static droplets of the intermediate-temperature tetragonal phase embedded within the high-temperature cubic phase, possibly nucleating about defects [25]. We observe no inelastic scattering at the R-points in both the INS or MD $S(\mathbf{Q} = (H, 1.5, 0.5), E)$ in Fig. 4b. Incoherent-background-subtracted energy scans at a constant \mathbf{Q} corresponding to R-points are best fit by a Gaussian lineshape with resolution limited linewidth (Fig. 4c), hence this scattering is static with $\xi = 2$ nm (Table S1),

consistent with previous reports [25]. These droplets are distinct from the 2D pancakes but we are not able to resolve the spatial distribution of these two components. We expect that both structures influence MA^+ orientation.

The appearance of small regions of a lower temperature phase above the phase transition temperature is often a hallmark of critical scattering. For phase transitions with critical fluctuations, there is a marked jump in intensity of the associated low temperature phase as the system is cooled through the transition [38]. We investigate the temperature dependence of the diffuse scattering in Figs. S13,14 through the cubic-tetragonal transition temperatures for MAPbI_3 and MAPbBr_3 . The intensity of the diffuse rods increases continuously with decreasing temperature through the transition, however no significant and abrupt jump in intensity is observed. Furthermore, the two-dimensional nature of the dynamic structural correlations is not typical of critical behavior at phase transitions. For the R-point scattering, however, there is a large jump in intensity as the cubic R-point transforms to the Γ -point of the tetragonal phase, giving Bragg scattering. The critical nature of the R-point scattering has been addressed previously [22, 25].

Our results show that the simple cubic phase of MAPbI_3 and MAPbBr_3 is in fact a composite structure containing dynamic 2D structural correlations and static tetragonal droplets with ξ of a few nanometers. MA^+ correlations, induced by octahedral tilts, extend 2-3 unit cells in the normal direction. The simple cubic phase is only recovered when this composite is averaged over space and time (Fig. 1 a-d). Structural fluctuations of lead halide octahedra generate large variations in the optical bandgap and electron-phonon coupling [9, 17, 24], therefore it is essential to incorporate the observed correlations when modeling optoelectronic properties. We expect the dynamic correlations and static droplets to introduce spatial anisotropy to the electronic potential landscape with a longer lifetime than variations resulting from uncorrelated dynamic disorder. Furthermore, we must consider the effect of local correlations of the organic sublattice on LHP properties. MA^+ has a large electric dipole moment of 2.3 Debye along the C-N axis [28]. Uncorrelated dynamic disorder of the MA^+ sublattice, as previously reported, would generate a zero or negligible dipole moment. The MA^+ correlations observed here, however, may generate a net dipole moment resulting in transient, local ferroelectric or antiferroelectric domains with lifetimes on the order of 3-6 ps. These domains influence electron-hole recombination and shift band alignment [39, 40]. The dynamic structural correlations also affect ion migration. In solid-state ion conductors, rotational dynamics of polyanions are known to strongly impact cation mobility [41]. Since the lifetime of the dynamic structural correlations (3-6 ps) exceeds the calculated time between attempted halide jumps (1 ps) [42], a prefactor in calculating diffusivity, the correlations appear static and must be considered in future calculations. These correlations may impose a barrier to halide migration and reduce diffusivity [27].

The two-dimensional dynamic structural correlations we observe may arise from the strongly anharmonic lattice dynamics observed in LHPs [29, 30, 35,

43]. Indeed, the structural correlations in CsPbBr₃ are reportedly driven by soft, overdamped, anharmonic phonons at the BZ edge [9]. We do not observe dispersive phonons along the BZ edge M-R branch in Fig. 4b, therefore these modes may be overdamped for MAPbI₃ and MAPbBr₃ as well. The structural correlations we observe on the PbX₆ sublattice have a longer lifetime than those in CsPbBr₃, and are prevalent at device relevant temperatures. The additional intermolecular correlations between MA⁺ are not present in CsPbBr₃ and contribute to the improved optoelectronic properties of hybrid LHPs.

1 Acknowledgements

The authors acknowledge helpful discussions with Xixi Qin, Volker Blum, and Alex Zunger. This work (X-ray and neutron scattering) was supported by the Center for Hybrid Organic Inorganic Semiconductors for Energy, and Energy Frontier Research Center funded by the Office of Basic Energy Sciences, an office of science within the US Department of Energy (DOE). J. A. V. acknowledges fellowship support from the Stanford University Office of the Vice Provost of Graduate Education and the National Science Foundation Graduate Research Fellowship Program under Grant No. DGE – 1656518. H. I. K. acknowledges funding through the DOE Office of Basic Energy Sciences, Division of Materials Science and Engineering, under Contract No. DE-AC02-76SF0051. T.C.S. and D.R. acknowledge funding by the DOE Office of Basic Energy Sciences, Office of Science, under Contract No. DE-SC0006939. A portion of this research used resources at the Spallation Neutron Source, a DOE Office of Science User Facility operated by the Oak Ridge National Laboratory. Use of the Advanced Photon Source at Argonne National Laboratory was supported by the U.S. Department of Energy, Office of Science, Office of Basic Energy Sciences, under Contract No. DE-AC02-06CH11357. Experiments at the ISIS Pulsed Neutron and Muon Source were supported by a beamtime allocation from the Science and Technology Facilities Council. Any mention of commercial products here is for information only; it does not imply recommendation or endorsement by the National Institute of Standards and Technology.

2 Methods

2.1 Single crystal growth

2.1.1 Materials

Methyl-d₃-amine (CD₃NH₂, 99 at. % D) was purchased from Sigma-Aldrich. Hydrobromic acid (concentrated HBr solution, 48 % in water) was purchased from Acros Organics. Hydroiodic acid (concentrated HI solution, ≥47 % in water with ≤1.5 % hypophosphorous acid) was purchased from Sigma-Aldrich. Methanol-d₄ and ethanol-d₆ were purchased from Acros Organics and Cambridge Isotope Laboratories, Inc., respectively, with ≥99 at. % D purity. PbI₂

(99.999+ %-Pb) and PbBr_2 (98+ %, extra pure) were purchased from Strem Chemicals, Inc. and Acros Organics, respectively. $\text{CH}_3\text{NH}_3\text{I}$ and $\text{CH}_3\text{NH}_3\text{Br}$ were purchased from Greatcell Solar Materials. All solvents were of reagent grade or higher purity and anhydrous solvents were stored over molecular sieves or used directly from a JC Meyer solvent purification system.

2.1.2 Synthesis of $\text{CD}_3\text{ND}_3\text{X}_3$ ($\text{X} = \text{Br}, \text{I}$)

Methyl- d_3 -amine was bubbled through ethanol (in a round bottom flask with flowing N_2 in the headspace) in an ice water bath under vigorous stirring for approximately 2 minutes. Excess concentrated HBr was subsequently added dropwise with stirring. After the solution warmed naturally to room temperature (RT), the solvent was removed under reduced pressure at 60 °C. The resulting oil was re-dissolved in anhydrous ethanol and the product, $\text{CD}_3\text{NH}_3\text{Br}$, was precipitated as a colorless solid upon addition of the solution to cold diethyl ether. The solid was isolated by vacuum filtration and subsequently re-dispersed, sonicated, and isolated from diethyl ether three times before drying the product overnight under reduced pressure.

Solid $\text{CD}_3\text{NH}_3\text{Br}$ was dissolved in ethanol- d_6 and stirred for 3 h at 60 °C before precipitating the product in anhydrous diethyl ether and removing excess solvent under reduced pressure. This hydrogen-deuterium exchange was repeated twice more before finally isolating and drying the product, $\text{CD}_3\text{ND}_3\text{Br}$, at 65 °C overnight.

The synthesis of $\text{CD}_3\text{ND}_3\text{I}$ followed an analogous procedure as for $\text{CD}_3\text{ND}_3\text{Br}$, except for the substitutions of: ethanol (or ethanol- d_6 during the exchange) for methanol (or methanol- d_4), and concentrated HBr for concentrated HI .

2.1.3 Crystallization of $\text{CD}_3\text{ND}_3\text{PbBr}_3$

Solid $\text{CD}_3\text{ND}_3\text{Br}$ (0.235 g, 2 mmol) and PbBr_2 (0.731 g, 2 mmol) were combined in 2 mL of anhydrous dimethylformamide and the mixture was sonicated for 20 minutes. Once dissolved, the solution was passed through a 0.22- μm hydrophilic PTFE filter and transferred to an oil bath at 78 °C. Crystals of $\text{CD}_3\text{ND}_3\text{PbBr}_3$ slowly nucleated at the interface between the solution and the surface of the vial as the temperature increased slowly (1-3 °C h^{-1}) from 78 °C (up to 85-100 °C). Crystals were isolated from the hot solution and the residual precursor solution was quickly removed from the surface of the crystal. Large crystals (≥ 200 mg) were obtained by isolating small crystals (25-50 mg) as seeds and re-filtering the precursor solution into a fresh vial with one seed crystal and quickly transferring back to the oil bath at 78 °C. Repeating the temperature ramp described above resulted in large crystal growth after a period of minor re-dissolution from the seed.

2.1.4 Crystallization of $\text{CH}_3\text{NH}_3\text{PbBr}_3$

A 1-M solution of $\text{CH}_3\text{NH}_3\text{Br}$ and PbBr_2 in anhydrous dimethylformamide was prepared and sonicated for 1 h. Then 1 mL of the precursor solution was passed through a glass microfiber filter and transferred to a shell vial. The shell vial was placed inside a larger vial containing 4 mL of dichloromethane, the anti-solvent for the vapor diffusion crystallization, and sealed. Millimeter-scale $(\text{CH}_3\text{NH}_3)\text{PbBr}_3$ crystals formed over the course of hours to days at room temperature.

2.1.5 Crystallization of $\text{CD}_3\text{ND}_3\text{PbI}_3$ and $\text{CH}_3\text{NH}_3\text{PbI}_3$

Solid $\text{CD}_3\text{ND}_3\text{I}$ (0.594 g, 3.6 mmol) and PbI_2 (1.66 g, 3.6 mmol) were combined in 3 mL of anhydrous γ -butyrolactone and dissolved at 70 °C with stirring. The solution was hot-filtered through a 0.22- μm PTFE filter and immediately transferred to an oil bath at 70 °C. The temperature was increased to 110 °C over the course of approximately 2 h, followed by a slow ramp (1-3 °C h^{-1}) up to 120-130 °C. Crystals were isolated and re-seeded as described for $\text{CD}_3\text{ND}_3\text{PbBr}_3$ to reach the desired size.

The crystallization of $\text{CH}_3\text{NH}_3\text{PbI}_3$ followed an analogous procedure as for $\text{CD}_3\text{ND}_3\text{PbI}_3$, except for the substitution of $\text{CD}_3\text{ND}_3\text{I}$ for $\text{CH}_3\text{NH}_3\text{I}$.

2.2 Diffuse X-ray scattering

Reciprocal space maps, including Bragg and diffuse scattering contributions, were collected in transmission geometry at the Advanced Photon Source Sector 6-ID-D using monochromatic 86.9 keV X-rays. This X-ray scattering is inherently energy integrated, incorporating contributions from both static and thermal diffuse disorder. Single crystal samples of $(\text{CD}_3\text{ND}_3)\text{PbI}_3$, $(\text{CH}_3\text{NH}_3)\text{PbI}_3$, and $(\text{CH}_3\text{NH}_3)\text{PbBr}_3$, $\sim 500\mu\text{m}$ in size were mounted on the tip of Kapton capillaries. At each temperature, the sample was rotated 365° at 1° s^{-1} with images collected every 0.1 s on a Pilatus 2M CdTe area detector. Sample temperatures were varied between 150 - 300 K with an Oxford N-Helix (check) Cryostream and 300 - 360 K with a hot nitrogen blower. The raw images are first processed with a peak finding algorithm to determine and refine an orientation matrix, and then rebinned into a reciprocal space volume ± 10 r.l.u. a side using the CCTW reduction workflow[4, 44]. The dataset is symmetrized using cubic point group operations to remove missing data resulting from gaps between detector pixel banks.

Sample damage is evident from changes in the scattering intensity with prolonged exposure. The damage thresholds were determined by identifying the onset of additional scattering intensity in subsequent measurements of the same sample at constant temperature. In MAPbI_3 , damage is apparent after 90 minutes of measurement time (including time when the shutter is off in between each rotation for data collection), therefore all diffuse scattering analyzed here was collected on a fresh sample within 90 minutes.

2.3 Diffuse neutron scattering

Neutron diffuse scattering measurements were performed on the CORELLI spectrometer at the Spallation Neutron Source at Oak Ridge National Lab in Oak Ridge, Tennessee, USA[11, 12]. Deuterated MAPbBr₃ (300, 350 mg, rectangular prism) and MAPbI₃ (220 mg, rhombic dodecahedron) crystals were used to reduce incoherent background contributions from hydrogen. The crystals were mounted in a CCR cryostat and oriented in the (HK0) scattering plane. The incident neutron energies range from 10 - 200 meV, and the 2θ coverage spans -30 to 145°. MAPbBr₃ scattering data was collected from 150 - 300 K for 4-6 hours per temperature, and MAPbI₃ scattering data was collected from 300 - 400 K at 12 hours per temperature to account for smaller sample size and increased background from the thermal shielding. Diffuse scattering volumes ± 6 r.l.u. a side were obtained by reducing the raw data using defined workflows implemented in MANTID[45]. The contributions from inelastic scattering are removed by implementing the cross-correlation technique in the MANTID reduction workflow. The cross-correlation chopper selects elastically scattered neutrons within a resolution bandwidth of 0.9 meV full-width at half maximum [12]. Background artefacts including the aluminum sample enclosure are removed by subtracting the highest temperature datasets (300 K for MAPbBr₃, 400 K for MAPbI₃), normalized by the Bragg peaks, where little to no diffuse scattering is detected.

2.4 Neutron inelastic scattering

Neutron inelastic scattering measurements were performed on the Merlin direct geometry chopper spectrometer at the ISIS Neutron and Muon source at the Rutherford Appleton Laboratory in Didcot, UK[46]. A deuterated single crystal of MAPbI₃ weighing 698 mg was oriented in the (HKK) scattering plane and mounted in a Brookhaven-style aluminum sample can. Temperature control was performed using a closed-cycle refrigerator with heaters attached directly to the sample can. Three incident energies of 11, 22, and 65 meV were selected by utilizing the repetition rate multiplication mode with the Fermi chopper set to 250 Hz. The $S(\mathbf{Q}, E)$ was collected at 340 K by rotating the sample 120° in 0.5° steps, and a radial collimator was used to reduce scattering from the aluminum sample can. Data reduction was performed using the HORACE data reduction suite and analyzed with Phonon Explorer and the National Institute of Standards and Technology (NIST) Center for Neutron Research (NCNR) Data Analysis and Visualization Environment (DAVE) software packages [47–50].

Energy scans for linewidth analysis were sliced from the 11 meV incident energy $S(\mathbf{Q}, E)$ dataset. The resolution linewidth of this dataset was determined from constant- \mathbf{Q} scans at \mathbf{Q} values unique to the aluminum Debye-Scherrer rings. Several constant- \mathbf{Q} scans obtained in this manner were fit to a Gaussian lineshape with constant background to obtain an average resolution linewidth of 0.5 meV FWHM. A representative constant- \mathbf{Q} scan was

used as the resolution function in subsequent analyses. The incoherent background was determined from constant- \mathbf{Q} scans at \mathbf{Q} values which contain only incoherent scattering with no contributions from diffuse rods, Bragg peaks, or aluminum Debye-Scherrer rings. Several background scans were averaged, then subtracted from the constant- \mathbf{Q} scans along the diffuse rods and at the R-point to remove the incoherent background contribution and isolate the dynamics associated with these features.

Additional high-resolution neutron spectroscopy was performed on the cold neutron triple-axis spectrometer (SPINS) at the NCNR in Gaithersburg, MD, USA. The same deuterated single crystal of MAPbI₃ weighing 698 mg was oriented in the (HKK) scattering plane and mounted in a Brookhaven-style aluminum sample can. Constant- \mathbf{Q} scans, in which we vary the energy transfer while maintaining constant momentum transfer \mathbf{Q} , were performed with a fixed final energy $E_F = 5$ meV. We compare constant- \mathbf{Q} scans taken along $\mathbf{Q} = (2, k, 0)$ and at $\mathbf{Q} = (1.5, 0, 0)$ at 300 and 140 K, to constant- \mathbf{Q} cuts calculated from the MD $S(\mathbf{Q}, E)$ as a way to validate the calculations.

2.5 Molecular dynamics simulations

MD trajectories for deuterated MAPbI₃ are generated using identical simulations to those in ref. [35] with the mass of hydrogen set to that of deuterium. We used a $20 \times 20 \times 10$ super-cell that is based on the 12-atom pseudocubic unit cell with cell length $a \approx 6.3$ Å. The simulations were done in the LAMMPS package [51]. The inter-atomic potential is from ref. [52]. Trajectories were integrated using a 0.5 fs time step throughout. For the first 20 ps, the system was thermalized in the NPT ensemble at 300 K and 0 Pa, then it was equilibrated for another 20 ps in the NVE ensemble. After equilibration, the equations of motion were integrated for 20 ns and trajectories were written to a file every 50 fs.

2.6 $S(\mathbf{Q}, E)$ calculations

The dynamical structure factor, $S(\mathbf{Q}, E)$, can be calculated from MD. Given a set of suitably accurate trajectories, $\mathbf{r}_i(t)$, $S(\mathbf{Q}, E)$ can be evaluated directly as

$$S(\mathbf{Q}, E) = \left| \sum_i^N f_i(Q) \int \exp(i(\mathbf{Q} \cdot \mathbf{r}_i(t) - \frac{E}{\hbar}t)) dt \right|^2. \quad (2)$$

See the supplementary information [34] and refs. therein [53–60] for a derivation of eq. 2. The theoretical $S(\mathbf{Q}, E)$ calculations were done with a Python code developed by us [61]. The calculated $S(\mathbf{Q}, E)$ is weighted by X-ray atomic form factors or thermal neutron scattering lengths for direct comparison to experimental data [54, 55]. If the experiment uses neutrons, $f_i(Q) \equiv b_i$ is the Q -independent scattering length; if the experiment uses X-rays, $f_i(Q)$ is the Q -dependent atomic form factor where Q is the magnitude of momentum

transferred, \mathbf{Q} , from the incident beam of particles into the material. E is the energy transferred into the material and the sum runs over all N atoms.

The reciprocal space resolution from MD is $\Delta Q_{H,K} \approx 0.05 \text{ \AA}^{-1}$ along the H , K directions and $\Delta Q_L \approx 0.1 \text{ \AA}^{-1}$ along the L direction. We do not integrate the calculation over reciprocal space unless otherwise specified, so the pixels in theoretical $S(\mathbf{Q}, E)$ plots have this spacing. In order to ensure we are far from the transient thermalization regime in MD, we only sample the last nano-second of the simulation to calculate $S(\mathbf{Q}, E)$. The last nano-second is split into 20 blocks that are 50 ps long; $S(\mathbf{Q}, E)$ is then calculated from 10 non-consecutive blocks and averaged over them. For 50 ps blocks with a 50 fs sampling interval, the energy resolution is about 0.08 meV and the maximum resolvable energy is 41.4 meV.

To compare to the experimental NDS data in Fig. 2, theoretical $S(\mathbf{Q}, E)$ is integrated between ± 0.5 meV, which is comparable to the resolution in the experiment. To compare to the experimental XDS data in Fig. 2, theoretical $S(\mathbf{Q}, E)$ is integrated between ± 2 meV. To compare with INS data in Fig. 4, both the experimental and theoretical $S(\mathbf{Q}, E)$ are integrated ± 1 meV. Anywhere that purely theoretical data is compared, the integration is ± 1 meV. For excitations [e.g. Fig. 4(b)], theoretical $S(\mathbf{Q}, E)$ is not integrated over energy; the MD energy resolution is set by the length of the trajectory sampled in the calculation.

The workflow and analysis outlined above was performed on MD simulations of protonated MAPbI₃ and no significant differences were observed. The deuterated results are used in the main text for direct comparison to the experimental measurements.

2.7 Plotting

The unit cells in Fig. 1a, b were plotted in VESTA [62]. The volumetric plot in Fig. 1e was made in MAYAVI [63]. Most other plots were made using the matplotlib package for Python [64].

3 Data and Software Availability

The experimental and computational datasets used in the analysis here will be made available upon reasonable request. INS data associated with this experiment will be made publicly available by the Science and Technology Facilities Council at DOI: 10.5286/ISIS.E.RB2010431 The code used to calculate $S(\mathbf{Q}, E)$ is available for free online [61].

4 Author Contributions

N.J.W., H.-G.S., and M.F.T. conceived the project. N.J.W., J.A.V., H.-G.S., F.Y., and M.J.K. performed the XDS and NDS experiments and data reduction and N.J.W., T.C.S., D.R., and M.F.T. performed the analysis. J.A.V., A.G.-P., I.C.S., and H.I.K. synthesized and mounted the single crystals. T.C.S.

performed and analyzed the $S(\mathbf{Q}, E)$ calculations from the MD datasets provided by B.A. and E.E. N.J.W., T.C.S., D.V., A.G.-P., I.C.S., P.M.G., and D.R. performed the INS experiments and contributed to the analysis. N.J.W. and T.C.S. prepared the figures and wrote the manuscript with contributions from all authors.

References

- [1] Ashcroft, N.W., Mermin, N.D.: Solid State Physics. Harcourt, New York (2000)
- [2] Kittel, C., McEuen, P., John Wiley & Sons.: Introduction to Solid State Physics. John Wiley & Sons, Hoboken, NJ (2019)
- [3] Clément, R.J., Lun, Z., Ceder, G.: Cation-disordered rocksalt transition metal oxides and oxyfluorides for high energy lithium-ion cathodes. *Energy & Environmental Science* **13**(2), 345–373 (2020). <https://doi.org/10.1039/C9EE02803J>
- [4] Krogstad, M.J., Rosenkranz, S., Wozniak, J.M., Jennings, G., Ruff, J.P.C., Vaughey, J.T., Osborn, R.: Reciprocal space imaging of ionic correlations in intercalation compounds. *Nature Materials* **19**(1), 63–68 (2020). <https://doi.org/10.1038/s41563-019-0500-7>
- [5] Simonov, A., De Baerdemaeker, T., Boström, H.L.B., Ríos Gómez, M.L., Gray, H.J., Chernyshov, D., Bosak, A., Bürgi, H.-B., Goodwin, A.L.: Hidden diversity of vacancy networks in Prussian blue analogues. *Nature* **578**(7794), 256–260 (2020). <https://doi.org/10.1038/s41586-020-1980-y>
- [6] Xu, G., Zhong, Z., Hiraka, H., Shirane, G.: Three-dimensional mapping of diffuse scattering in $\text{Pb}(\text{Zn}_{1/3}\text{Nb}_{2/3})\text{O}_3-x\text{PbTiO}_3$. *Physical Review B* **70**(17), 174109 (2004). <https://doi.org/10.1103/PhysRevB.70.174109>
- [7] Krogstad, M.J., Gehring, P.M., Rosenkranz, S., Osborn, R., Ye, F., Liu, Y., Ruff, J.P.C., Chen, W., Wozniak, J.M., Luo, H., Chmaissem, O., Ye, Z.-G., Phelan, D.: The relation of local order to material properties in relaxor ferroelectrics. *Nature Materials* **17**(8), 718–724 (2018). <https://doi.org/10.1038/s41563-018-0112-7>
- [8] Roth, N., Zhu, T., Iversen, B.B.: A simple model for vacancy order and disorder in defective half-Heusler systems. *IUCrJ* **7**(4), 673–680 (2020). <https://doi.org/10.1107/S2052252520005977>
- [9] Lanigan-Atkins, T., He, X., Krogstad, M.J., Pajerowski, D.M., Abernathy, D.L., Xu, G.N.M.N., Xu, Z., Chung, D.-Y., Kanatzidis, M.G., Rosenkranz, S., Osborn, R., Delaire, O.: Two-dimensional overdamped fluctuations of the soft perovskite lattice in CsPbBr_3 . *Nature Materials*, 1–7 (2021).

<https://doi.org/10.1038/s41563-021-00947-y>

- [10] Welberry, T.R., Weber, T.: One hundred years of diffuse scattering. *Crystallography Reviews* **22**(1), 2–78 (2016). <https://doi.org/10.1080/0889311X.2015.1046853>
- [11] Rosenkranz, S., Osborn, R.: Corelli: Efficient single crystal diffraction with elastic discrimination. *Pramana* **71**(4), 705–711 (2008). <https://doi.org/10.1007/s12043-008-0259-x>
- [12] Ye, F., Liu, Y., Whitfield, R., Osborn, R., Rosenkranz, S.: Implementation of cross correlation for energy discrimination on the time-of-flight spectrometer CORELLI. *Journal of Applied Crystallography* **51**(2), 315–322 (2018). <https://doi.org/10.1107/S160057671800403X>
- [13] Proffen, T., Kim, H.: Advances in total scattering analysis. *Journal of Materials Chemistry* **19**(29), 5078–5088 (2009). <https://doi.org/10.1039/B821178G>
- [14] Simonov, A., Weber, T., Steurer, W.: Yell: A computer program for diffuse scattering analysis via three-dimensional delta pair distribution function refinement. *Journal of Applied Crystallography* **47**(3), 1146–1152 (2014). <https://doi.org/10.1107/S1600576714008668>
- [15] Morgan, Z.J., Zhou, H.D., Chakoumakos, B.C., Ye, F.: Rmc-discord: Reverse Monte Carlo refinement of diffuse scattering and correlated disorder from single crystals. *Journal of Applied Crystallography* **54**(6), 1867–1885 (2021). <https://doi.org/10.1107/S1600576721010141>
- [16] Egger, D.A., Bera, A., Cahen, D., Hodes, G., Kirchartz, T., Kronik, L., Lovrincic, R., Rappe, A.M., Reichman, D.R., Yaffe, O.: What Remains Unexplained about the Properties of Halide Perovskites? *Advanced Materials* **30**(20), 1800691 (2018). <https://doi.org/10.1002/adma.201800691>
- [17] Mayers, M.Z., Tan, L.Z., Egger, D.A., Rappe, A.M., Reichman, D.R.: How Lattice and Charge Fluctuations Control Carrier Dynamics in Halide Perovskites. *Nano Letters* **18**(12), 8041–8046 (2018). <https://doi.org/10.1021/acs.nanolett.8b04276>
- [18] Weller, M.T., Weber, O.J., Henry, P.F., Pumpo, A.M.D., Hansen, T.C.: Complete structure and cation orientation in the perovskite photovoltaic methylammonium lead iodide between 100 and 352 K. *Chemical Communications* **51**(20), 4180–4183 (2015). <https://doi.org/10.1039/C4CC09944C>
- [19] Whitfield, P.S., Herron, N., Guise, W.E., Page, K., Cheng, Y.Q., Milas, I., Crawford, M.K.: Structures, Phase Transitions and Tricritical Behavior of

- the Hybrid Perovskite Methyl Ammonium Lead Iodide. *Scientific Reports* **6**, 35685 (2016). <https://doi.org/10.1038/srep35685>
- [20] Swainson, I.P., Hammond, R.P., Soullière, C., Knop, O., Massa, W.: Phase transitions in the perovskite methylammonium lead bromide, CH₃ND₃PbBr₃. *Journal of Solid State Chemistry* **176**(1), 97–104 (2003). [https://doi.org/10.1016/S0022-4596\(03\)00352-9](https://doi.org/10.1016/S0022-4596(03)00352-9)
- [21] Beecher, A.N., Semonin, O.E., Skelton, J.M., Frost, J.M., Terban, M.W., Zhai, H., Alatas, A., Owen, J.S., Walsh, A., Billinge, S.J.L.: Direct Observation of Dynamic Symmetry Breaking above Room Temperature in Methylammonium Lead Iodide Perovskite. *ACS Energy Letters* **1**(4), 880–887 (2016). <https://doi.org/10.1021/acsenerylett.6b00381>
- [22] Comin, R., Crawford, M.K., Said, A.H., Herron, N., Guise, W.E., Wang, X., Whitfield, P.S., Jain, A., Gong, X., McGaughey, A.J.H., Sargent, E.H.: Lattice dynamics and the nature of structural transitions in organolead halide perovskites. *Physical Review B* **94**(9), 094301 (2016). <https://doi.org/10.1103/PhysRevB.94.094301>
- [23] Laurita, G., Fabini, D.H., Stoumpos, C.C., Kanatzidis, M.G., Seshadri, R.: Chemical tuning of dynamic cation off-centering in the cubic phases of hybrid tin and lead halide perovskites. *Chemical Science* **8**(8), 5628–5635 (2017). <https://doi.org/10.1039/C7SC01429E>
- [24] Zhao, X.-G., Dalpian, G.M., Wang, Z., Zunger, A.: Polymorphous nature of cubic halide perovskites. *Physical Review B* **101**(15), 155137 (2020). <https://doi.org/10.1103/PhysRevB.101.155137>
- [25] Weadock, N.J., Gehring, P.M., Gold-Parker, A., Smith, I.C., Karunadasa, H.I., Toney, M.F.: Test of the Dynamic-Domain and Critical Scattering Hypotheses in Cubic Methylammonium Lead Triiodide. *Physical Review Letters* **125**(7), 075701 (2020). <https://doi.org/10.1103/PhysRevLett.125.075701>
- [26] Yuan, Y., Huang, J.: Ion Migration in Organometal Trihalide Perovskite and Its Impact on Photovoltaic Efficiency and Stability. *Accounts of Chemical Research* **49**(2), 286–293 (2016). <https://doi.org/10.1021/acs.accounts.5b00420>
- [27] Holekevi Chandrappa, M.L., Zhu, Z., Fenning, D.P., Ong, S.P.: Correlated Octahedral Rotation and Organic Cation Reorientation Assist Halide Ion Migration in Lead Halide Perovskites. *Chemistry of Materials* **33**(12), 4672–4678 (2021). <https://doi.org/10.1021/acs.chemmater.1c01175>
- [28] Chen, T., Chen, W.-L., Foley, B.J., Lee, J., Ruff, J.P.C., Ko, J.Y.P., Brown, C.M., Harriger, L.W., Zhang, D., Park, C., Yoon, M., Chang,

- Y.-M., Choi, J.J., Lee, S.-H.: Origin of long lifetime of band-edge charge carriers in organic–inorganic lead iodide perovskites. *Proceedings of the National Academy of Sciences* **114**(29), 7519–7524 (2017). <https://doi.org/10.1073/pnas.1704421114>
- [29] Ferreira, A.C., Létoublon, A., Paofai, S., Raymond, S., Ecolivet, C., Rufflé, B., Cordier, S., Katan, C., Saidaminov, M.I., Zhumekenov, A.A., Bakr, O.M., Even, J., Bourges, P.: Elastic Softness of Hybrid Lead Halide Perovskites. *Physical Review Letters* **121**(8), 085502 (2018). <https://doi.org/10.1103/PhysRevLett.121.085502>
- [30] Gold-Parker, A., Gehring, P.M., Skelton, J.M., Smith, I.C., Parshall, D., Frost, J.M., Karunadasa, H.I., Walsh, A., Toney, M.F.: Acoustic phonon lifetimes limit thermal transport in methylammonium lead iodide. *Proceedings of the National Academy of Sciences* **115**(47), 11905–11910 (2018). <https://doi.org/10.1073/pnas.1812227115>
- [31] Leguy, A.M.A., Frost, J.M., McMahon, A.P., Sakai, V.G., Kockelmann, W., Law, C., Li, X., Foglia, F., Walsh, A., O’Regan, B.C., Nelson, J., Cabral, J.T., Barnes, P.R.F.: The dynamics of methylammonium ions in hybrid organic–inorganic perovskite solar cells. *Nature Communications* **6**, 7124 (2015). <https://doi.org/10.1038/ncomms8124>
- [32] Chen, T., Foley, B.J., Ipek, B., Tyagi, M., Copley, J.R.D., Brown, C.M., Choi, J.J., Lee, S.-H.: Rotational dynamics of organic cations in the $\text{CH}_3\text{NH}_3\text{PbI}_3$ perovskite. *Physical Chemistry Chemical Physics* **17**(46), 31278–31286 (2015). <https://doi.org/10.1039/C5CP05348J>
- [33] Guo, Y., Yaffe, O., Paley, D.W., Beecher, A.N., Hull, T.D., Szpak, G., Owen, J.S., Brus, L.E., Pimenta, M.A.: Interplay between organic cations and inorganic framework and incommensurability in hybrid lead-halide perovskite $\text{CH}_3\text{NH}_3\text{PbBr}_3$. *Physical Review Materials* **1**(4), 042401 (2017). <https://doi.org/10.1103/PhysRevMaterials.1.042401>
- [34] See Supplemental Material at [URL will be inserted by publisher] for derivation of $S(Q,E)$ from MD as well as other supporting information.
- [35] Zhu, T., Ertekin, E.: Mixed phononic and non-phononic transport in hybrid lead halide perovskites: glass-crystal duality, dynamical disorder, and anharmonicity. *Energy & Environmental Science* **12**(1), 216–229 (2019). <https://doi.org/10.1039/C8EE02820F>
- [36] Lahnsteiner, J., Kresse, G., Kumar, A., Sarma, D., Franchini, C., Bokdam, M.: Room-temperature dynamic correlation between methylammonium molecules in lead-iodine based perovskites: An ab initio molecular dynamics perspective. *Physical Review B* **94**(21), 214114 (2016). <https://doi.org/10.1103/PhysRevB.94.214114>

- [37] Vale, J.G., Boseggia, S., Walker, H.C., Springell, R.S., Hunter, E.C., Perry, R.S., Collins, S.P., McMorro, D.F.: Critical fluctuations in the spin–orbit Mott insulator $\text{Sr}_3\text{Ir}_2\text{O}_7$. *Journal of Physics: Condensed Matter* **31**(18), 185803 (2019). <https://doi.org/10.1088/1361-648X/ab0471>
- [38] Stirling, W.G., Perry, S.C.: Critical scattering. In: *Introduction to Neutron Scattering*, pp. 86–102 (1996)
- [39] Bi, F., Markov, S., Wang, R., Kwok, Y., Zhou, W., Liu, L., Zheng, X., Chen, G., Yam, C.: Enhanced Photovoltaic Properties Induced by Ferroelectric Domain Structures in Organometallic Halide Perovskites. *The Journal of Physical Chemistry C* **121**(21), 11151–11158 (2017). <https://doi.org/10.1021/acs.jpcc.7b03091>
- [40] Liu, Y., Collins, L., Proksch, R., Kim, S., Watson, B.R., Doughty, B., Calhoun, T.R., Ahmadi, M., Ievlev, A.V., Jesse, S., Retterer, S.T., Belianinov, A., Xiao, K., Huang, J., Sumpter, B.G., Kalinin, S.V., Hu, B., Ovchinnikova, O.S.: Chemical nature of ferroelastic twin domains in $\text{CH}_3\text{NH}_3\text{PbI}_3$ perovskite. *Nature Materials* **17**(11), 1013–1019 (2018). <https://doi.org/10.1038/s41563-018-0152-z>
- [41] Smith, J.G., Siegel, D.J.: Low-temperature paddlewheel effect in glassy solid electrolytes. *Nature Communications* **11**(1), 1483 (2020). <https://doi.org/10.1038/s41467-020-15245-5>
- [42] Frost, J.M., Walsh, A.: What Is Moving in Hybrid Halide Perovskite Solar Cells? *Accounts of Chemical Research* **49**(3), 528–535 (2016). <https://doi.org/10.1021/acs.accounts.5b00431>
- [43] Songvilay, M., Giles-Donovan, N., Bari, M., Ye, Z.-G., Minns, J.L., Green, M.A., Xu, G., Gehring, P.M., Schmalzl, K., Ratcliff, W.D., Brown, C.M., Chernyshov, D., van Beek, W., Cochran, S., Stock, C.: Common acoustic phonon lifetimes in inorganic and hybrid lead halide perovskites. *Physical Review Materials* **3**(9), 093602 (2019). <https://doi.org/10.1103/PhysRevMaterials.3.093602>
- [44] Cctw. <https://sourceforge.net/projects/cctw/>
- [45] Arnold, O., Bilheux, J.C., Borreguero, J.M., Buts, A., Campbell, S.I., Chapon, L., Doucet, M., Draper, N., Ferraz Leal, R., Gigg, M.A., Lynch, V.E., Markvardsen, A., Mikkelsen, D.J., Mikkelsen, R.L., Miller, R., Palmen, K., Parker, P., Passos, G., Perring, T.G., Peterson, P.F., Ren, S., Reuter, M.A., Savici, A.T., Taylor, J.W., Taylor, R.J., Tolchenov, R., Zhou, W., Zikovsky, J.: Mantid—Data analysis and visualization package for neutron scattering and μ SR experiments. *Nuclear Instruments and Methods in Physics Research Section A: Accelerators, Spectrometers, Detectors and Associated Equipment* **764**, 156–166 (2014). <https://doi.org/10.1016/j.nucinst.2014.05.011>

[//doi.org/10.1016/j.nima.2014.07.029](https://doi.org/10.1016/j.nima.2014.07.029)

- [46] Bewley, R.I., Eccleston, R.S., McEwen, K.A., Hayden, S.M., Dove, M.T., Bennington, S.M., Treadgold, J.R., Coleman, R.L.S.: MERLIN, a new high count rate spectrometer at ISIS. *Physica B: Condensed Matter* **385–386**, 1029–1031 (2006). <https://doi.org/10.1016/j.physb.2006.05.328>
- [47] Ewings, R.A., Buts, A., Le, M.D., van Duijn, J., Bustinduy, I., Per-ring, T.G.: Horace: Software for the analysis of data from single crystal spectroscopy experiments at time-of-flight neutron instruments. *Nuclear Instruments and Methods in Physics Research Section A: Accelerators, Spectrometers, Detectors and Associated Equipment* **834**, 132–142 (2016). <https://doi.org/10.1016/j.nima.2016.07.036>
- [48] Reznik, D., Ahmadova, I.: Automating Analysis of Neutron Scattering Time-of-Flight Single Crystal Phonon Data. *Quantum Beam Science* **4**(4), 41 (2020). <https://doi.org/10.3390/qubs4040041>
- [49] Reznik, D.: Phonon-Explorer. <https://github.com/dmitryr1234/Phonon-Explorer>
- [50] Azuah, R.T., Kneller, L.R., Qiu, Y., Tregenna-Piggott, P.L.W., Brown, C.M., Copley, J.R.D., Dimeo, R.M.: DAVE: A comprehensive software suite for the reduction, visualization, and analysis of low energy neutron spectroscopic data. *Journal of Research of the National Institute of Standards and Technology* **114**, 341–358 (2009). <https://doi.org/10.6028/jres.114.025>
- [51] Plimpton, S.: Fast parallel algorithms for short-range molecular dynamics. *Journal of computational physics* **117**(1), 1–19 (1995). <https://doi.org/10.1006/jcph.1995.1039>
- [52] Mattoni, A., Filippetti, A., Saba, M., Delugas, P.: Methylammonium rotational dynamics in lead halide perovskite by classical molecular dynamics: the role of temperature. *The Journal of Physical Chemistry C* **119**(30), 17421–17428 (2015). <https://doi.org/10.1021/acs.jpcc.5b04283>
- [53] Dove, M.T., Dove, M.T.: *Introduction to Lattice Dynamics*. Cambridge university press, Cambridge, United Kingdom (1993). <https://doi.org/10.1017/CBO9780511619885>
- [54] Brown, P., Fox, A., Maslen, E., O’keefe, M., Willis, B.: Intensity of diffracted intensities. In: *International Tables for Crystallography vol. C*, pp. 554–595. Wiley Online Library, Hoboken, NJ, United States (2006). Chap. 6.1. <https://doi.org/10.1107/97809553602060000600>
- [55] Hazemann, I., Dauvergne, M., Blakeley, M., Meilleur, F., Haertlein, M.,

- Van Dorsselaer, A., Mitschler, A., Myles, D.A., Podjarny, A.: High-resolution neutron protein crystallography with radically small crystal volumes: application of perdeuteration to human aldose reductase. *Acta Crystallographica Section D: Biological Crystallography* **61**(10), 1413–1417 (2005). <https://doi.org/10.1107/S0907444905024285>
- [56] Squires, G.L.: *Introduction to the Theory of Thermal Neutron Scattering*. Cambridge University Press, Cambridge, United Kingdom (2012). <https://doi.org/10.1017/CBO9781139107808>
- [57] Harrelson, T.F., Dettmann, M., Scherer, C., Andrienko, D., Moulé, A.J., Faller, R.: Computing inelastic neutron scattering spectra from molecular dynamics trajectories. *Scientific reports* **11**(1), 1–12 (2021). <https://doi.org/10.1038/s41598-021-86771-5>
- [58] Zushi, T., Ohmori, K., Yamada, K., Watanabe, T.: Effect of a SiO_2 layer on the thermal transport properties of $< 100 >$ Si nanowires: A molecular dynamics study. *Physical Review B* **91**(11), 115308 (2015). <https://doi.org/10.1103/PhysRevB.91.115308>
- [59] Xiong, S., Selli, D., Neogi, S., Donadio, D.: Native surface oxide turns alloyed silicon membranes into nanophononic metamaterials with ultralow thermal conductivity. *Physical Review B* **95**(18), 180301 (2017). <https://doi.org/10.1103/PhysRevB.95.180301>
- [60] Van Hove, L.: Correlations in space and time and Born approximation scattering in systems of interacting particles. *Physical Review* **95**(1), 249 (1954). <https://doi.org/10.1103/PhysRev.95.249>
- [61] Sterling, T.C.: *Pynamic Structure Factor*. <https://github.com/tyst3273/pynamic-structure-factor>
- [62] Momma, K., Izumi, F.: VESTA 3 for three-dimensional visualization of crystal, volumetric and morphology data. *Journal of Applied Crystallography* **44**(6), 1272–1276 (2011). <https://doi.org/10.1107/S0021889811038970>
- [63] Ramachandran, P., Varoquaux, G.: Mayavi: 3d visualization of scientific data. *Computing in Science & Engineering* **13**(2), 40–51 (2011). <https://doi.org/10.1109/MCSE.2011.35>
- [64] Hunter, J.D.: Matplotlib: A 2d graphics environment. *Computing in Science Engineering* **9**(3), 90–95 (2007). <https://doi.org/10.1109/MCSE.2007.55>

Supplementary Material for “The nature of
dynamic local order in $\text{CH}_3\text{NH}_3\text{PbI}_3$ and
 $\text{CH}_3\text{NH}_3\text{PbBr}_3$ ”

Nicholas J Weadock^{1,2*†}, Tyler C Sterling^{3†}, Julian A
Vigil^{4,5}, Aryeh Gold-Parker⁵, Ian C Smith⁵, Ballal
Ahammed⁶, Matthew J Krogstad⁷, Feng Ye⁸, David
Voneshen^{9,10}, Peter M Gehring, Hans-Georg Steinrück¹², Elif
Ertekin⁶, Hemamala I Karunadasa^{5,13}, Dmitry Reznik^{3*}
and Michael F Toney^{1,2,14*}

¹Materials Science and Engineering, University of Colorado,
Boulder, Boulder, CO, 80309, USA.

²Department of Chemical and Biological Engineering, University
of Colorado, Boulder, Boulder, CO, 80309, USA.

³Department of Physics, University of Colorado, Boulder,
Boulder, CO, 80309, USA.

⁴Department of Chemical Engineering, Stanford University,
Stanford, CA, 94305, USA.

⁵Department of Chemistry, Stanford University, Stanford, CA,
94305, USA.

⁶Department of Mechanical Science & Engineering and Materials
Research Laboratory, University of Illinois at
Urbana-Champaign, Urbana, IL, 61801, USA.

⁷Advanced Photon Source, Argonne National Lab, Lemont, IL,
60439, USA.

⁸Neutron Scattering Division, Oak Ridge National Laboratory,
Oak Ridge, TN, 37830, USA.

⁹ISIS Facility, Rutherford Appleton Laboratory, Chilton, Didcot,
Oxon OX11 0QX, United Kingdom.

¹⁰Department of Physics, Royal Holloway University of London,
Egham TW20 0EX, United Kingdom.

¹¹NIST Center for Neutron Research, National Institute of
Standards and Technology, Gaithersburg, MD, 20899, USA.

¹²Department Chemie, Universität Paderborn, Paderborn,
Germany.

¹³Stanford Institute for Materials and Energy Sciences, SLAC
National Accelerator Laboratory, Menlo Park, CA, 94025, USA.

¹⁴Renewable and Sustainable Energy Institute (RASEI),
University of Colorado, Boulder, Boulder, CO, 80303, USA.

*Corresponding author(s). E-mail(s):
nicholas.weadock@colorado.edu; dmitry.reznik@colorado.edu;
michael.toney@colorado.edu;

†These authors contributed equally to this work.

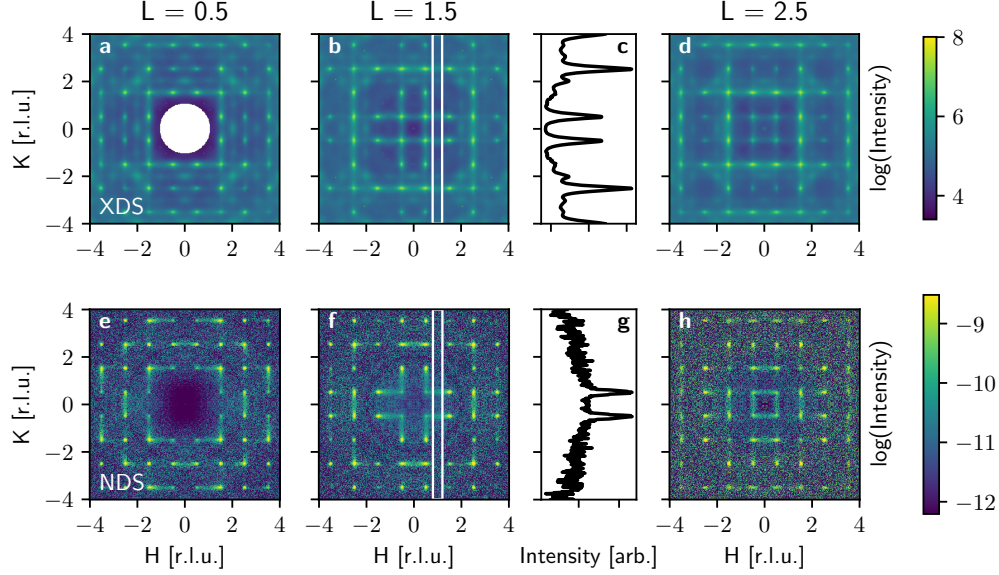


Fig. 1 Experimental $S(\mathbf{Q})$ for protonated (a-d) and deuterated (e-h) MAPbBr_3 measured at 250 K (globally cubic phase) with X-ray and neutron diffuse scattering, respectively. The NDS data are limited to the elastic scattering channel of the CORELLI spectrometer (0.9 meV FWHM), whereas the XDS data are inherently energy integrated. Reciprocal space slices taken at $L=0.5, 1.5, 2.5$ contain only diffuse scattering intensity. Linecuts in c, g, are obtained by integrating within the white boxes in b, f, respectively, and illustrate the difference in diffuse scattering intensities in XDS and NDS. The intensity in a,b,d,e,f,h is plotted on a logarithmic scale.

1 Diffuse scattering of MAPbBr_3

Representative slices of the reciprocal space volumes collected for MAPbBr_3 using X-ray (XDS) and neutron diffuse scattering (NDS) are plotted in Figure S1. Cuts in the H, K, L=0.5, 1.5, and 2.5 planes show diffuse scattering patterns nearly identical to MAPbI_3 , namely extended (XDS) or modulated (NDS) rods of intensity along the Brillouin Zone (BZ) edge connecting the M and R-points. One-dimensional cuts in \mathbf{Q} in Fig. S1c,g highlight the alternating intensity profile of NDS.

2 $S(\mathbf{Q}, E)$ from molecular dynamics

We derive the equation used to calculate the dynamic structure factor, $S(\mathbf{Q}, E)$, from molecular dynamics.

The dynamic structure factor is defined as

$$\begin{aligned}
 S(\mathbf{Q}, \omega) &= \int \int \langle \hat{\rho}(\mathbf{r} + \mathbf{r}', t + t') \hat{\rho}(\mathbf{r}', t') \rangle \exp(i(\mathbf{Q} \cdot \mathbf{r} - \omega t)) dt d\mathbf{r} \\
 &\equiv \int G(\mathbf{r}, t) \exp(i(\mathbf{Q} \cdot \mathbf{r} - \omega t)) dt d\mathbf{r} \\
 &\equiv \int F(\mathbf{Q}, t) \exp(-i\omega t) dt
 \end{aligned} \tag{1}$$

Eq. 1 is the time- and space-Fourier transform of the density-density correlation function (also called the *Van Hove* function [1]), $G(\mathbf{r}, t)$. $\hat{\rho}(\mathbf{r}, t)$ is the quantum mechanical density operator, by necessity defined using a quantum mechanical position operator $\hat{\mathbf{r}}_i(t)$.

Positions do not commute at different times t, t' therefore evaluating Eq. 1 is difficult. To simplify the notation, we do not write the explicit time dependence of $\hat{\mathbf{r}}$ except where it is needed. The usual method to evaluate Eq. 1 for crystals is to expand the position operators, $\hat{\mathbf{r}}$, in terms of the phonon creation and annihilation operators [2]. This works well when the harmonic approximation is sufficient, but at high-temperatures and particularly in molecular crystals where molecules rotate almost freely, this is not adequate. Instead, we approximate the positions as classical coordinates so that $\hat{\rho} \equiv \rho$ is classical and the classical positions $\mathbf{r}(t)$ can be determined using molecular dynamics simulations¹. Importantly we have made no assumptions about the configuration of the material, so this computational technique is valid for liquids, disordered compounds, molecular crystals, etc. The main source of error of the classical approximation is that the scattering function $S(\mathbf{Q}, \omega)$ does not satisfy the principle of detailed balance [2–4].

Still, we use the classical approximation for ρ in all places where $S(\mathbf{Q}, \omega)$ is calculated from molecular dynamics trajectories in the text. The classical approximation becomes valid at high-temperature where quantum effects on nuclear motion are negligible.

For classical (i.e. commuting) positions, Eq. 1 can be simplified. With

$$\delta(\mathbf{r} - \mathbf{r}_i) = \int \exp(-i\mathbf{Q}' \cdot (\mathbf{r} - \mathbf{r}_i)) \frac{d\mathbf{Q}'}{(2\pi)^3} \quad (2)$$

we can write $\rho(\mathbf{r}, t)$ as [3]

$$\rho(\mathbf{r}, t) = \sum_i^N f_i(Q) \int \exp(-i\mathbf{Q}' \cdot (\mathbf{r} - \mathbf{r}_i)) \frac{d\mathbf{Q}'}{(2\pi)^3}. \quad (3)$$

In Eq. 3 $f_i(Q) \equiv b_i$ is the \mathbf{Q} -independent neutron scattering length if the experiment uses neutrons; if X-rays are used, then $f_i(Q)$ is the \mathbf{Q} -dependent atomic form factor which can be approximated by a sum of Gaussians

$$f_i(Q) = \sum_j^4 p_{i,j} \exp\left(-q_{i,j} \left(\frac{Q}{4\pi}\right)^2\right) + s_i. \quad (4)$$

The parameters $p_{i,j}$, $q_{i,j}$, and s_i for X-rays and the scattering lengths b_i for neutrons have already been determined and tabulated [5, 6]. The index i runs over all atoms in the compound and $f_i(Q)$ is different for different atoms.

¹Ab-initio molecular dynamics works as well because the atomic trajectories are classical.

Q is the (magnitude of-) momentum transferred from the incident (monochromatic) beam into the sample.

The classical expression for the Van Hove function, $G(\mathbf{r}, t)$ in Eq. 1, is

$$G(\mathbf{r}, t) = \langle \rho(\mathbf{r} + \mathbf{r}', t + t') \rho(\mathbf{r}', t') \rangle = \int \int \rho(\mathbf{r} + \mathbf{r}', t + t') \rho(\mathbf{r}', t') d\mathbf{r}' dt'. \quad (5)$$

Inserting Eq. 3 into Eq. 5 and carrying out the integrals, we find

$$G(\mathbf{r}, t) = \sum_i^N \sum_j^N f_i(Q) f_j(Q) \int \delta(\mathbf{r} - (\mathbf{r}_i(t + t') - \mathbf{r}_j(t'))) dt'. \quad (6)$$

Similarly, inserting Eq. 6 into Eq. 1, we find:

$$F(\mathbf{Q}, t) = \sum_i^N \sum_j^N f_i(Q) f_j(Q) \int \exp(i\mathbf{Q} \cdot (\mathbf{r}_i(t + t') - \mathbf{r}_j(t'))) dt'. \quad (7)$$

Next, we can rewrite $\exp(i\mathbf{Q} \cdot \mathbf{r}(t))$ as

$$\exp(i\mathbf{Q} \cdot \mathbf{r}(t)) = \int \exp(i\mathbf{Q} \cdot \mathbf{r}(\tau)) \delta(\tau - t) d\tau. \quad (8)$$

Combining equations 7 and 8 with Eq. 1, we can do all the integrals over exponentials:

$$S(\mathbf{Q}, \omega) = \sum_i^N \sum_j^N f_i(Q) f_j(Q) \int \int \exp(i(\mathbf{Q} \cdot \mathbf{r}_i(\tau) - \omega\tau)) \times \exp(-i(\mathbf{Q} \cdot \mathbf{r}_j(\tau') - \omega\tau')) d\tau d\tau'. \quad (9)$$

Finally, with $E \equiv \hbar\omega$ and $\tau \equiv t$, we can rewrite this as

$$S(\mathbf{Q}, E) = \left| \sum_i^N f_i(Q) \int \exp(i(\mathbf{Q} \cdot \mathbf{r}_i(t) - \frac{E}{\hbar}t)) dt \right|^2. \quad (10)$$

Equation 10 can be evaluated from molecular dynamics trajectories, $\mathbf{r}_i(t)$. An expression similar to Eq. 9 has been used in the past [7, 8].

3 How well do MD and experiment agree?

The relative scale of the theoretical and experimental $S(\mathbf{Q}, E)$ is arbitrary since there are no incident X-ray or neutron fluxes in the MD simulation and this quantity was not explicitly measured in the experiments. Moreover, there are background contributions from the experimental setup that are not present

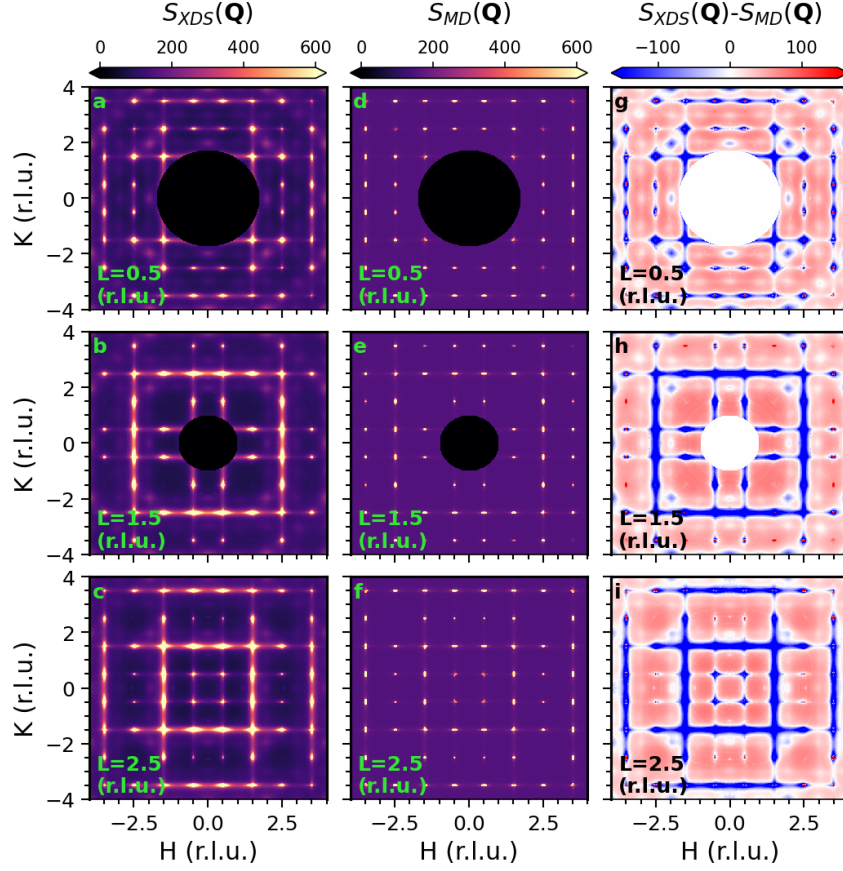


Fig. 2 Difference between XDS for MAPbI₃ at 345 K and “best-fit” MD data at 300 K. The MD data in d-f have a constant offset of 151.25 and scale of 40.22, determined by minimizing the RMS error with these as parameters. The RMS error is 91.78 (3.9% of the maximum, 2164.92). The error, $S_{\text{XDS}}(\mathbf{Q}) - S_{\text{MD}}(\mathbf{Q})$, for each L are in g-i.

in MD. In the comparisons between the calculated and experimental $S(\mathbf{Q}, E)$ in the main text, the calculated data are multiplied by an arbitrary scaling factor to account for these differences and to allow a qualitative comparison. To obtain a more quantitative measure of the accuracy of our MD results, we calculate the root-mean-squared (RMS) error between experimental and computed $S(\mathbf{Q})$, adjusted for a constant background and scaled for incident flux. First, we consider the agreement in two dimensions for the $L = 0.5$, 1.5, and 2.5 scattering planes. The background offset and scale are varied to minimize the RMS error. Data in a sphere around $\mathbf{Q} = (0, 0, 0)$ were removed from the MD data because there are no data here in the XDS experiment. The results of “fitting” the MD data to experiment in the $L = 0.5$, 1.5, 2.5 r.l.u. planes are shown in Fig. S2. The scale and offset are summarized in the caption.

In Fig. S2 we calculate the RMS error as 91.78 (3.9% of the maximum in XDS data, 2164.92). A particular source of error is the “empty” space between diffuse rods; the experimental data are not constant here, but we approximate the background as constant in the comparison. Comparing the data near the

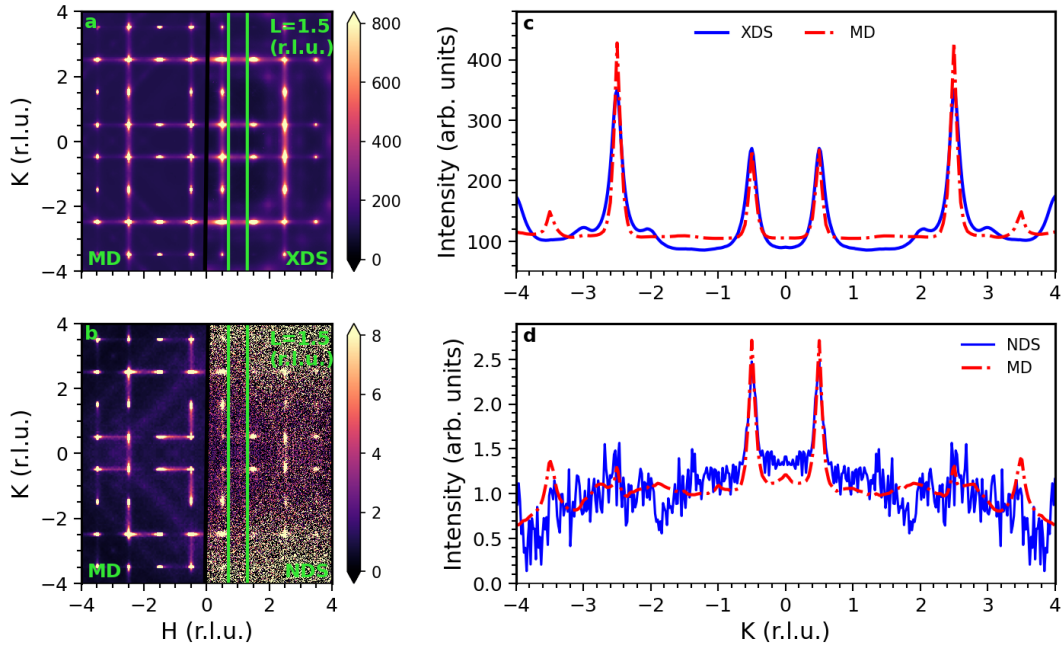


Fig. 3 Linecut across the diffuse rods highlighting the agreement between MD and experiment. a Diffuse scattering from MAPbI_3 in the $L = 1.5$ plane from MD (left) and XDS at 345 K (right). c A linecut through the intensity in a. Data in c are integrated over the region between the vertical lines in a [$0.7 < H < 1.3$, K , $1.4 < L < 1.6$ r.l.u.]. The height and scale of the MD data in c were fit to the XDS data with an RMS error of 6.8%. b Diffuse scattering in the $L = 1.5$ plane from MD (left) and MAPbI_3 NDS at 345 K (right). d A linecut through the same region as in c comparing calculated and MD NDS data. The height and scale of the MD data in d were fit to the NDS data with an RMS error of 10.1%. The MD data in a and b are scaled using the results of the fits in c and d. In c, the peaks at integer values of K in the XDS data are likely phonons.

zone-boundaries shows that the R -points in the MD data are more intense than the diffuse-rods: the R -points are very bright in the MD figures (linear scale), while the rods are almost invisible. This is apparent in Fig. S2g-i, where the intensity at the R -points is too large, and the intensity near the diffuse rods is too low. This is likely an artifact of the difference in simulation temperature (300 K) and measurement temperature (345 K and above), as the R -point intensity increases with decreasing temperature [9–11].

We also compare MD data and experiment using linecuts across diffuse rods in Fig. S3. In this case, the fitting results in RMS error of 6.8% and 10.1% for XDS and NDS, respectively. The MD is scaled by the parameters obtained in the linecut fits and representative scattering in the $L = 1.5$ plane is presented in Fig. S3 a and b. Qualitatively, the MD and XDS, NDS have better visual agreement than in Fig. S2 in which whole planes are considered for the fit. In particular, we find that the diffuse rods look nearly identical between MD and experiment in Fig. S2a. Since we are mainly interested in the diffuse rods, in the main text we vary the scale and background of the calculated $S(\mathbf{Q})$ to highlight these features. We note that scaling by the Bragg intensity is not possible as the Bragg intensities measured in XDS can saturate

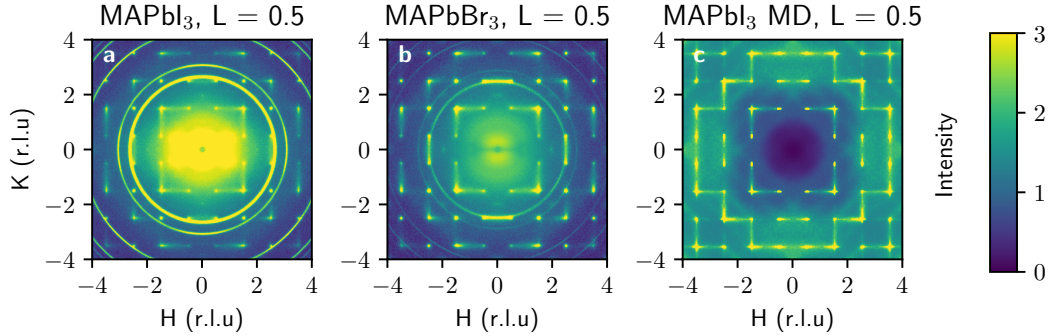


Fig. 4 Experimental neutron diffuse scattering in the $L = 0.5$ plane for a, MAPbI₃ at 345 K; b, MAPbBr₃ at 250 K; and c, MD calculated NDS for MAPbI₃. In a,b, we note that the diffuse intensity along the rods decays away from one of the two R-point endpoints. The Debye-Scherrer powder rings from the aluminum are subtracted in Fig. 2 in the main text and Fig. S1 for clarity but do not alter the diffuse scattering intensity.

the Pilatus detector pixels and therefore does not provide an accurate measure of the intensity.

We qualitatively compare the experimental and calculated NDS in Fig. S4. A quantitative comparison is difficult due to the significant Debye-Scherrer rings from the aluminum sample holder used in NDS. The alternating nature of the intensity along the diffuse rods is well reproduced for smaller H, K, values in the $L = 0.5$ plane, however there is reduced intensity in the experimental NDS for rods originating from the $\mathbf{Q} = (3.5, 3.5, 0.5)$ and $\mathbf{Q} = (1.5, 3.5, 0.5)$ families of R-points. This is apparent for both MAPbI₃ and MAPbBr₃, and indicates that the intermolecular correlations are not as strong as predicted by the MD. Our simulations utilize a classical, electrostatic potential which has been demonstrated to accurately, but not perfectly, model the experimental molecular relaxation times of MA⁺ [12]. The simulation also does not capture defects or thermally excited carriers which could screen electrostatic interactions between MA⁺.

4 Intensity variation along the rods

We note in the main text that the XDS and NDS diffuse rods have qualitatively different intensity profiles: the magnitude of XDS intensity is relatively constant along several BZs, whereas for NDS the intensity is reduced for every other BZ as observed in Figs. S1 and S4. Furthermore, along individual BZ edges the NDS diffuse intensity decays from the R-point (Fig. S4). By contrast, the XDS intensity is constant except for the R-point contribution. Fig. S5 plots linecuts along the diffuse rods for the 354 K XDS data along $\mathbf{Q} = (2.5, k, 0.5)$, $(0.5, k, 1.5)$ and $(1.5, k, 2.5)$ in a,b,c, respectively. Linecuts along the rods extracted from the MD X-ray and neutron $S(\mathbf{Q})$ are also plotted for comparison. We see the experimental and MD XDS intensity is constant between the R-points, whereas the NDS intensity falls off asymmetrically between the

R-points. Since XDS shows no variation along the rod and NDS does, the variation in NDS likely arises from scattering from the MA^+ molecules which are nearly invisible to X-rays. We verify this below.

The sublattice contributions to the diffuse scattering intensity are analyzed in the following way. Denoting $\rho(\mathbf{Q}, E) = \sum_i f_i(Q) \int \exp(i(\mathbf{Q} \cdot \mathbf{r}_i(t) - tE/\hbar)) dt$ with i labeling the atom and the sum running over all atoms in a particular group, we separate the intensity into terms corresponding to the inorganic PbI_6 (cage) and organic (MA^+) sublattices:

$$\begin{aligned} S(\mathbf{Q}, E) &= |\rho_{\text{MA}}(\mathbf{Q}, E) + \rho_{\text{cage}}(\mathbf{Q}, E)|^2 \\ &= |\rho_{\text{MA}}(\mathbf{Q}, E)|^2 + |\rho_{\text{cage}}(\mathbf{Q}, E)|^2 \\ &\quad + \rho_{\text{MA}}^*(\mathbf{Q}, E)\rho_{\text{cage}}(\mathbf{Q}, E) + \rho_{\text{cage}}^*(\mathbf{Q}, E)\rho_{\text{MA}}(\mathbf{Q}, E) \end{aligned} \quad (11)$$

where $\rho_{\text{MA}}(\mathbf{Q}, E)$ and $\rho_{\text{cage}}(\mathbf{Q}, E)$ are only summed over the atoms in the groups denoted by the subscript: MA^+ (methylammonium) are C, D (deuterium), and N atoms while cage atoms are Pb and I. We call $|\rho_{\text{MA}}(\mathbf{Q}, E = 0)|^2 \equiv S_{\text{MA}}(\mathbf{Q})$ and similarly for the cage atoms. The interference term is calculated from $S_{\text{int.}}(\mathbf{Q}) = S(\mathbf{Q}) - (S_{\text{MA}}(\mathbf{Q}) + S_{\text{cage}}(\mathbf{Q}))$.

The different contributions to $S(\mathbf{Q})$ are plotted in Fig. S6. We find that $S_{\text{cage}}(\mathbf{Q})$ is nearly indistinguishable from the calculated X-ray intensity (Fig. S6 g-i). i.e. the XDS measurement only probes the correlations of the PbI_6 octahedra. We also extract linecuts from each $S(\mathbf{Q})$ contribution along $Q = (2.5, k, 0.5)$, $(0.5, k, 1.5)$ and $(1.5, k, 2.5)$ and plot them in Fig. S7. The linecuts corresponding to $S_{\text{cage}}(\mathbf{Q})$ are in good agreement with the experimental and MD XDS in Fig. S5. Moreover, because the XDS and cage-only intensities show these rods of constant intensity (Figs. S5,S7), it is clear that the PbI_6 octahedra structural correlations have a two-dimensional character.

The plots of $S_{\text{MA}}(\mathbf{Q})$ in Figs. S6 and S7 show two components of MA^+ diffuse scattering. First is the broad, spherical component corresponding to uncorrelated disorder arising from such molecular reorientations as rotations of methyl or amine groups about the C-N axis of MA^+ . This component manifests as the nearly isotropic, circular intensity in Fig. S6d-f. Second are the strong, distinct diffuse rods with varying intensity along the rod direction. The rods orient parallel to one of the H,K,L directions and indicate the presence of intermolecular structural correlations similar to the pancakes of tilted PbI_6 octahedra. The varying intensity, however, implies that the intermolecular correlations extend beyond one unit cell in the out-of-plane direction. Due to the nonzero $S_{\text{int.}}(\mathbf{Q})$ term, there is no clear way to isolate intermolecular MA^+ correlation lengths from the experimental or calculated diffuse scattering. Instead, we evaluate it explicitly below from the MD trajectories.

The interference term $S_{\text{int.}}(\mathbf{Q})$ is plotted in Figs. S7, S8 and indicates that the separate sublattice correlations are connected to one another. If they were entirely uncorrelated, $S_{\text{int.}}(\mathbf{Q}) = 0$ everywhere and the total $S(\mathbf{Q}) = S_{\text{cage}}(\mathbf{Q}) + S_{\text{MA}}(\mathbf{Q})$. Instead, there are regions of constructive and destructive interference, with the constructive component resembling the total NDS

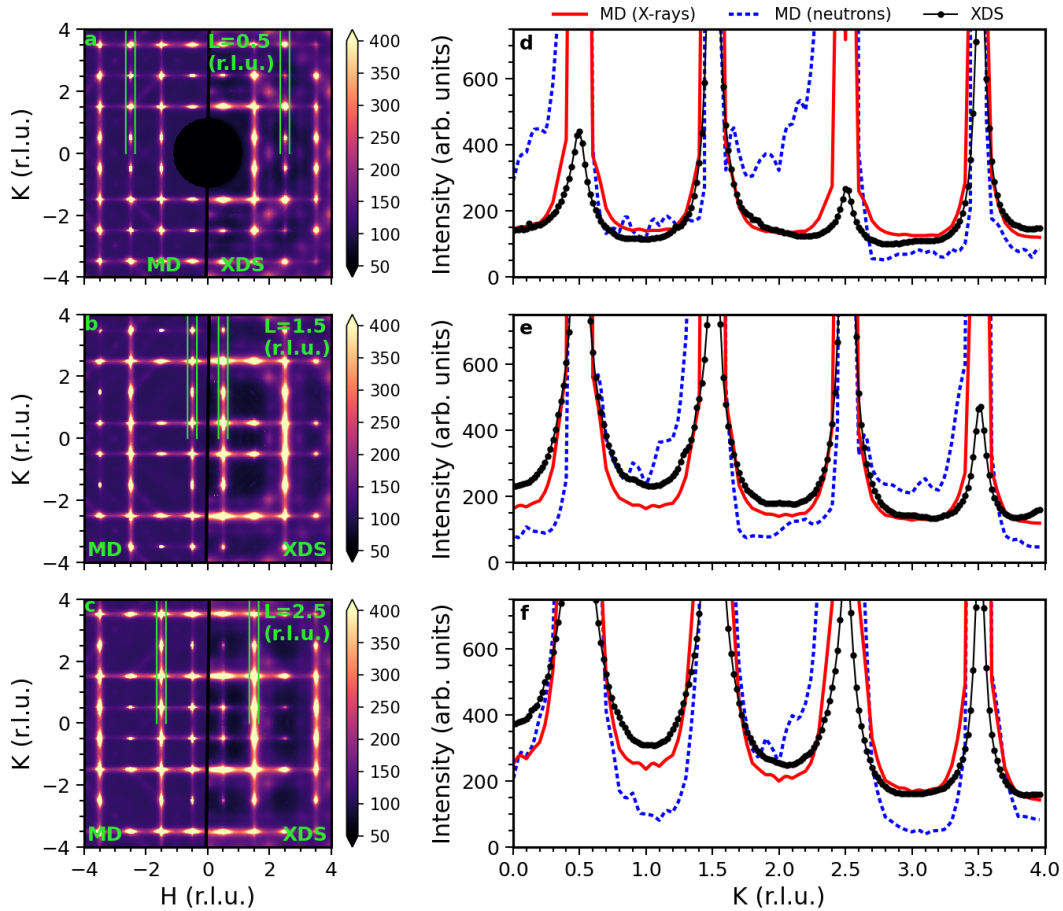


Fig. 5 Comparison between the diffuse intensity along the rods in in MAPbI₃ from MD and XDS at 345 K. The MD data (with X-ray form-factors) are on the left and XDS data on the right in a-c. Linecuts integrated between the green lines in a-c are plotted in d-f; MD (X-ray) data are red lines, MD (with neutron scattering lengths) are blue dotted lines, and the XDS data are black dots. MD (neutron) data are not plotted in a-c but provided for comparison. See Fig. 6 for the corresponding data. The shift and scale applied to the MD data is the same as determined in Fig. S3. The XDS data in d-f are integrated ± 0.5 r.l.u. while the MD are not integrated over momentum.

intensity (a-c in Fig. S6). We propose that the structural correlations between the two sublattices result from MA⁺ molecules reorienting into the lowest energy configuration in the cubocathedral region between PbI₆ octahedra, as discussed in the Main Text.

5 Correlation lengths

Correlation lengths ξ , corresponding to the widths of the two-dimensional structural correlations, are evaluated as stated in the Main Text and reported in Table S1 below. For XDS experiments the ξ correspond to PbX₆ correlations only, because the X-ray scattering intensity from light elements like C, N, D is significantly weaker.

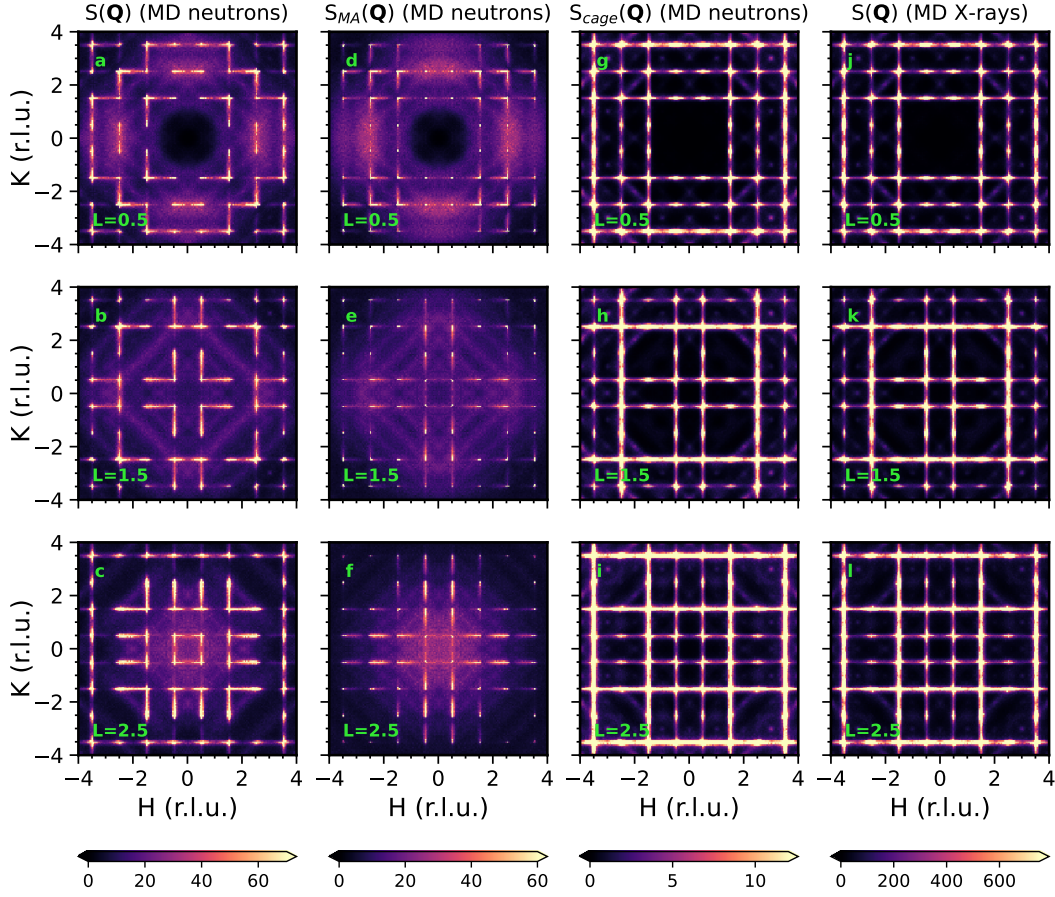


Fig. 6 Different sublattice contributions to the total diffuse scattering intensity calculated from MD. The total NDS intensity is in a-c and the total XDS intensity is in j-l. Scattering from only the MA and cage sublattices is in d-f and g-i, respectively.

In addition to determining the PbI_6 correlation lengths from the diffuse scattering data, we evaluate the PbI_6 and MA^+ ξ directly from the MD trajectories. To do this, we define a general correlation function between two dynamical variables, $\alpha(\mathbf{r}, t)$ and $\beta(\mathbf{r}, t)$ as [13]

$$G_{\alpha\beta}(\mathbf{r}, t) = \langle \alpha(\mathbf{r}, t) \beta(0, 0) \rangle = \int \alpha(\mathbf{r}', t') \beta(\mathbf{r} + \mathbf{r}', t + t') d\mathbf{r}' dt'. \quad (12)$$

The space-integral at equal time extends over the entire volume of the simulation box and the time integral over a long enough period to sample the correlations adequately. For a system with long-range order, $G_{\alpha\beta}(\mathbf{r}, t)$ will be finite at infinite distance, whereas a system with short-range order exhibits a peak which decays towards zero at large \mathbf{r} and t .

For the PbI_6 correlations, we use the “in-plane” iodine atom displacements, $\delta u_z(\mathbf{r}, t)$, as dynamical variables (see Fig. S9). The in-plane displacement is defined as that of the iodine atom perpendicular to the Pb-I bond arising from rotations of the octahedra about the axis perpendicular to the plane. We limit our analysis to displacements in the $x-y$ plane; i.e. rotations about the z -axis,

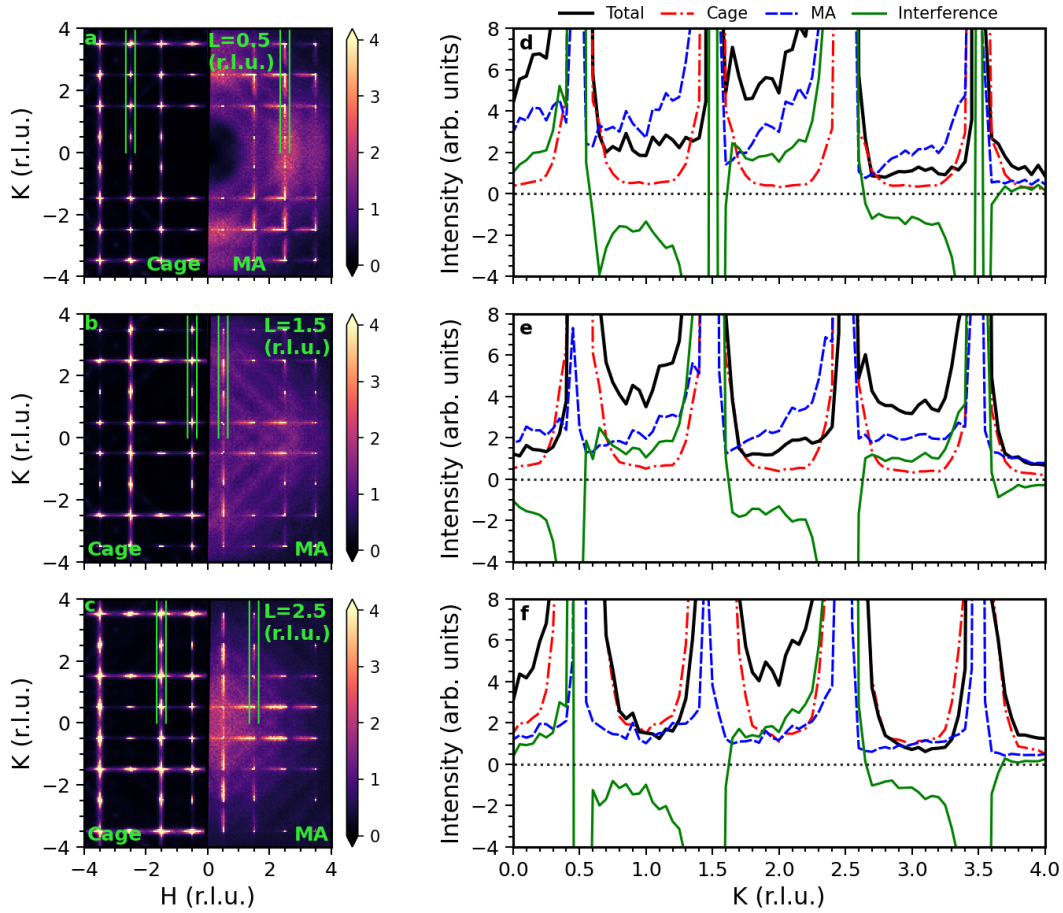


Fig. 7 Different sublattice contributions to the intensity along the diffuse rods in MAPbI₃ from MD. The cage and MA⁺ sublattice contributions to the theoretical neutron scattering intensity, $S_{\text{cage}}(\mathbf{Q})$ and $S_{\text{MA}}(\mathbf{Q})$, are on the left and right respectively in a-c. In d-f, the cage and MA⁺ contributions are labeled in the legend above. Also shown are the total intensity and interference components from MD. The MD data are integrated ± 0.5 meV.

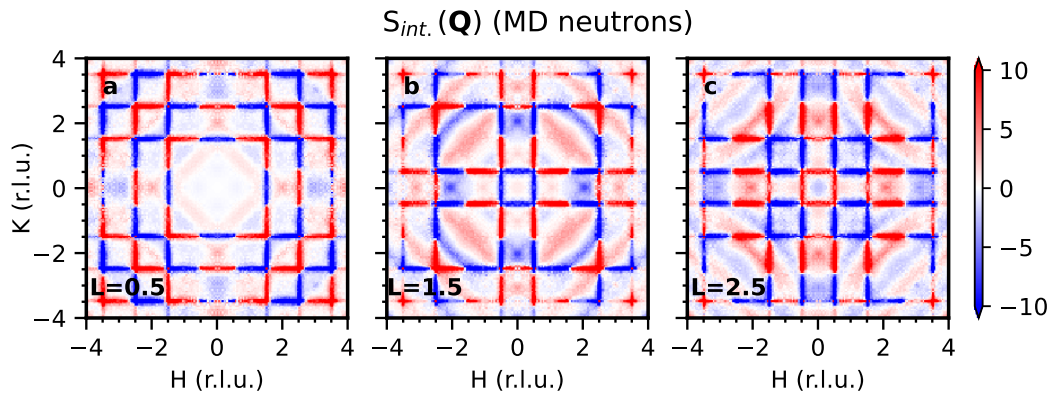


Fig. 8 The interference part of $S(\mathbf{Q})$ calculated from MD. The data in a are in the $L = 0.5$ r.l.u. plane, in b are in the $L = 1.5$ r.l.u. plane, and in c are in the $L = 2.5$ r.l.u. plane.

Table 1 Correlation lengths obtained from \mathbf{Q} linewidths of the diffuse rods and R-points. We report average values and standard deviation determined from several diffuse rods or R-points. For all R-point linewidths fitted here, contributions from the diffuse rod intensity have been subtracted prior to fitting. All reported lengths are in \AA , and correspond to the radius of the structural correlation.

	MAPbBr ₃		MAPbI ₃				
	250 K XDS ¹	NDS	330 K XDS	335 K NDS	345 K XDS	NDS	360 K XDS
Diffuse rods	10(2)	10(2)	13(4)	15(4)	12(3)	15(8)	11(3)
R-points	19(2)	17(7)	23(4)	25(7)	19(4)	21(6)	17(2)

¹Experiments performed on protonated MAPbBr₃.

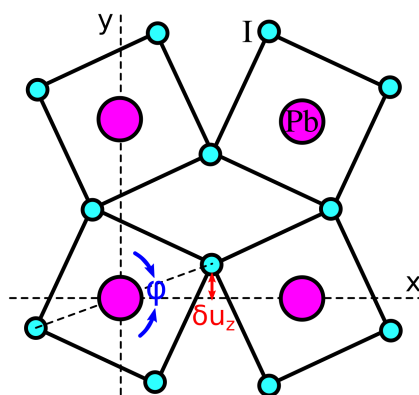


Fig. 9 Diagram depicting the dynamical variable $\delta u_z(\mathbf{r}, t)$ for explicit calculation of the PbI_6 correlations. δu_z are the displacements of the iodine atoms due to rotation of the octahedra about the z -axis by angles ϕ .

but note that these correlations are present within the $y-z$ and $z-x$ planes as well, as discussed in the Main Text. We define $\delta u_z(\mathbf{r}, t) = \sum_i \delta(\mathbf{r} - \mathbf{r}_i) \sin(\phi_i(t))$ with the bond-length set to unity and the octahedra fixed at the center of the unitcell. Thus, the PbI_6 correlation function only incorporates azimuthal rotations of the octahedra.

In the case of the MA^+ cations, the variables $\alpha(\mathbf{r}, t)$ and $\beta(\mathbf{r}, t)$ are the Cartesian components of the MA^+ molecular orientation: $\mathbf{n}(\mathbf{r}, t) = n_x(\mathbf{r}, t)\hat{\mathbf{x}} + n_y(\mathbf{r}, t)\hat{\mathbf{y}} + n_z(\mathbf{r}, t)\hat{\mathbf{z}}$. The vectors $\mathbf{n}_i(t)$ are parallel to the relative position vector between the C and N atoms belonging to the same MA^+ cation. The orientation field is $\mathbf{n}(\mathbf{r}, t) \equiv \sum_i \mathbf{n}_i(t)\delta(\mathbf{r} - \mathbf{r}_i)$ with \mathbf{r}_i the center-of-mass coordinate of the molecule. The sum runs over all MA^+ cations in the simulation cell (using periodic boundary conditions). For simplicity, we also assume $\mathbf{n}_i(t)$ are dimensionless unit vectors and that their centers-of-mass are fixed at the unit cell center. This isolates the MA^+ correlation function to measuring the MA^+ orientations only.

Eq. 12 can be evaluated directly, but the computational cost scales poorly with system size and time interval. It is more efficient to evaluate in reciprocal space where, by the convolution theorem, convolution (e.g. eq. 12) becomes

simple multiplication. The reciprocal space analogue of eq. 12 is

$$G_{\alpha\beta}(\mathbf{q}, \omega) = \alpha^*(\mathbf{q}, \omega)\beta(\mathbf{q}, \omega). \quad (13)$$

$\alpha(\mathbf{q}, \omega)$ is the space and time Fourier transform of the $\alpha(\mathbf{r}, t)$ and similarly for $\beta(\mathbf{q}, \omega)$. * denotes complex conjugation. The real space version is recovered by inverse Fourier transforming (assuming the volume and time interval are infinite for notational convenience):

$$G_{\alpha\beta}(\mathbf{r}, t) = \int G_{\alpha\beta}(\mathbf{q}, \omega) \exp(-i\mathbf{q} \cdot \mathbf{r} + i\omega t) \frac{d\omega}{2\pi} \frac{d\mathbf{q}}{(2\pi)^3}. \quad (14)$$

Eq. 14 is efficiently evaluated using numerical fast Fourier transforms.

The PbI_6 correlations in Fig. S10 exhibit a localized peak superposed with an oscillatory or constant offset. The offset corresponds to partial long-range order arising from a population of PbI_6 octahedra with non-zero tilts. We note that these tilt angles are less than those observed within the 2D pancakes, as reflected in the Main Text Fig. 3, and therefore the correlations in Fig. S10 are smaller at longer length scales. Along the in-plane lattice vector (Fig. S10a), neighboring octahedra rotate in opposite directions as required by the PbI_6 bond coupling them. As a result, the correlations alternate between positive and negative for each successive unit cell. Similarly, along the in-plane diagonal, neighboring octahedra rotate in the same direction (Fig. S10b), so there are no negative correlations. The ξ are determined by fitting an exponential plus an oscillatory or constant offset depending on the direction. The in-plane ξ are both $\sim 10 \text{ \AA}$, close to the $12(3) \text{ \AA}$ determined by fitting the diffuse rods in the XDS data.

Along the out-of-plane direction, Fig. S10c, the localized peak is extremely narrow: less than a unit cell. Two fit results are presented; $\xi = 0.50 \text{ \AA}$ and $\xi = 1.00 \text{ \AA}$. The peak is too narrow to fit reliably, but $\xi = 1.00 \text{ \AA}$ puts an upper bound on the out-of-plane ξ . Since the dynamical variables for the PbI_6 correlations are the in-plane iodine displacements, larger correlations correspond to displacements of similar magnitude. Thus, the largest peaks in Fig. S10 correspond to localized regions of octahedra with similar tilts. These extend several unit cells in the in-plane direction but only a single unit cell in the out-of-plane direction. Moreover, the in-plane ξ in Fig. S10a, b, are nearly identical, suggesting the correlated regions are nearly circular. The correlations in these PbI_6 calculations correspond to the 2D pancakes with large octahedral tilts as discussed in the Main Text.

At a glance, the equal time MA^+ correlations in Fig. S11 look like narrow, sharp peaks indicating primarily uncorrelated orientations with exponential decay. The peaks are fit as $\exp(-|r|/\xi)$ with correlation lengths of $1/2$ a unit cell. However, we expect the MA^+ correlations to have ξ similar to those measured experimentally ($\sim 15 \text{ \AA}$, see Table S 1).

Correlation lengths of $\sim 1/2$ a unit cell are inconsistent with this. However, there is a small, additional component to the MA^+ correlations with a

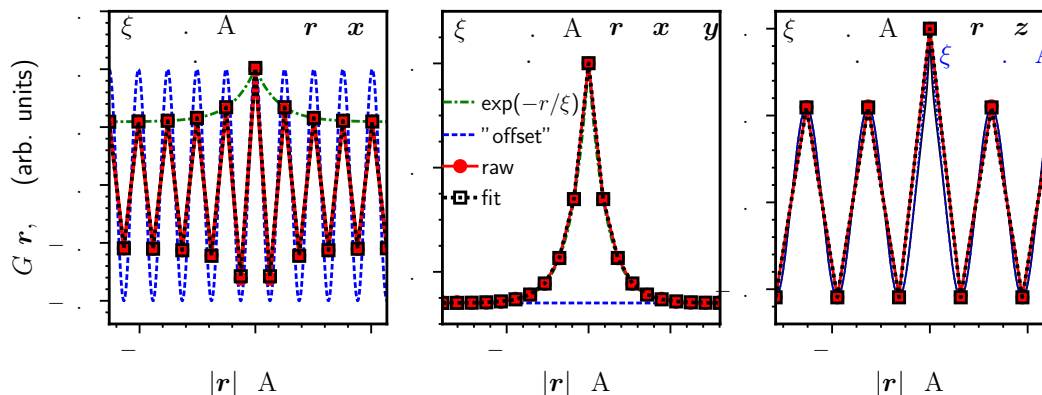


Fig. 10 Equal-time correlations of the PbI_6 rotations along an in-plane lattice vector a , along the in-plane diagonal b , and along the axis perpendicular to the plane c . Components of the fit are plotted as dashed (offset) and dot-dash ($\exp(-|r|/\xi)$) lines as detailed in b. The correlation lengths, ξ , are plotted with each panel. In c, the results of two separate fits to lead to the same RMS error, putting the upper bound on the correlation length at $\sim 1 \text{ \AA}$. There are fewer data points in c due to the supercell size along this dimension.

second length scale, highlighted in Fig. S12 which expands the y-axis. Here, we fit two exponential decays and, where appropriate, an oscillatory or constant background to the correlations. The fit is improved and RMS error reduced. The longer length scale is $\sim 15 \text{ \AA}$, corresponding to in-plane MA^+ correlations consistent with both the PbI_6 2D pancakes discussed above and the experimental data.

In ref. [12], MAPbI_3 was simulated using the same MD potential and the *time* correlations of the MA^+ orientations are fit to a model including *three* time scales: (i) diffusive dynamics of coupled molecules, (ii) free rotation of the molecules, and (iii) coupling of the molecules to phonons. The local 2D nature of the PbI_6 dynamics were unknown at the time, so it is unclear if one of the three time scales corresponds to the pancakes. Still, direct comparison of the time correlation curves in Figs. S11c, SS12c to those in reference. [12] reveals very good agreement. The short ranged component could be related to free rotation of the molecules or to inter-molecular interactions.

6 Energy linewidths from MD

In Fig. 13 we show the results of fitting Lorentzian functions to $S(\mathbf{Q}, E)$ calculated from MD to determine theoretical energy linewidths at the R-point and along a diffuse rod. The MD lifetimes are compared to experiment in Fig. 4 in the main text. MD predicts lifetimes consisted with those observed in the experiment.

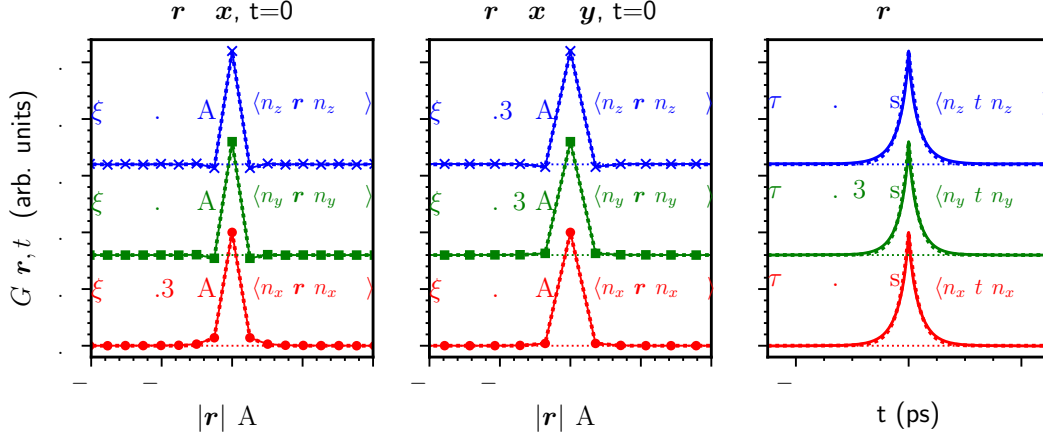


Fig. 11 Equal-time correlations of the MA^+ orientations along a lattice vector \mathbf{a} , along the diagonal spanned by two lattice vectors \mathbf{b} , and at equal-position but separated in time \mathbf{c} . Correlations between Cartesian components of the MA^+ orientation vector are labeled $\langle n_i(\mathbf{r})n_i(0) \rangle$ with i labeling the component. The correlation length, ξ , and correlation times, τ , are plotted in the panels.

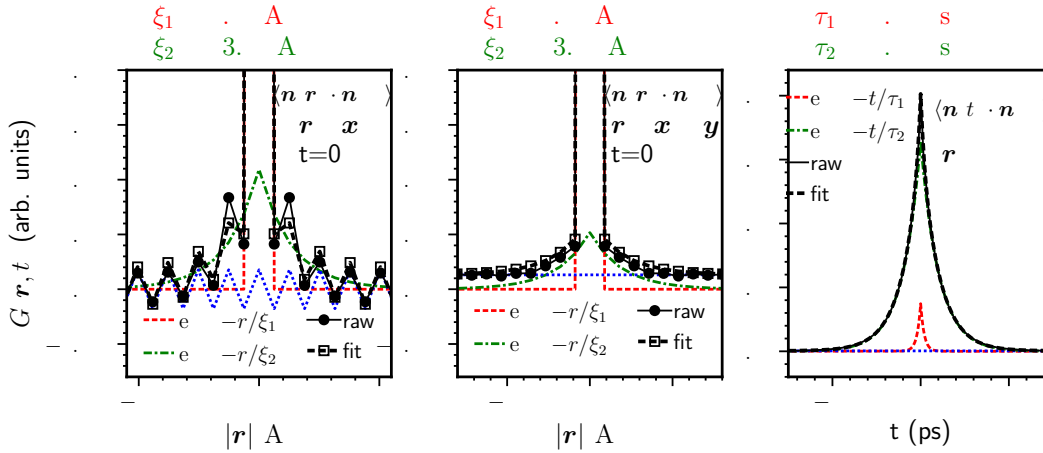


Fig. 12 Equal-time correlations of the MA^+ orientations along a lattice vector \mathbf{a} , along the diagonal spanned by two lattice vectors \mathbf{b} , and at equal-position but separated in time \mathbf{c} . Only the dot products $\langle \mathbf{n}(\mathbf{r}) \cdot \mathbf{n}(0) \rangle = \langle \sum_{i=0}^3 n_i(\mathbf{r})n_i(0) \rangle$ are shown. The y -axis scale is set to highlight the long-ranged length scale component of the correlations. The two correlation lengths, ξ_1 and ξ_2 , and the correlation times, τ_1 and τ_2 , are plotted in the panels.

7 Temperature dependence of diffuse scattering

We examine the temperature dependence of the diffuse scattering intensity as a way to distinguish between thermal diffuse (phonon) and static diffuse contributions. Phonons obey Bose-Einstein statistics with their thermal occupation $\langle n \rangle$ determined by the Bose-Einstein distribution:

$$\langle n \rangle = \frac{1}{\exp\left(\frac{\hbar\omega}{k_{\text{B}}T}\right) - 1} \quad (15)$$

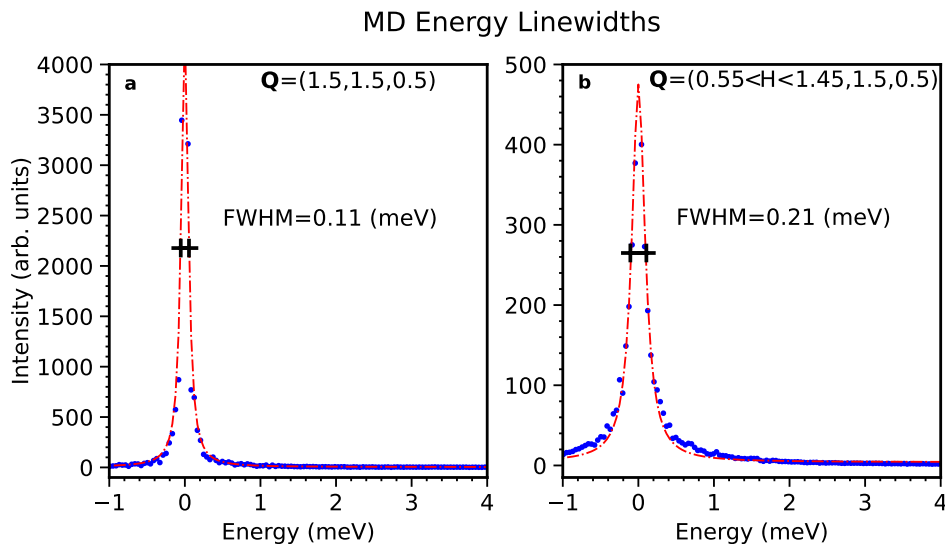


Fig. 13 Energy linewidth fits to simulated INS intensity calculated from MD at the R-point, a, and to calculated intensity integrated along a diffuse rod, b. The data in a are integrated between (1.45:H:1.55, 1.45:K:1.55, 0.45:L:0.55) and in b between (0.55:H:1.45, 1.45:K:1.55, 0.45:L:0.55). The lineshapes are assumed to be Lorentzian. The FWHM's are shown by the markers and labels in the plots.

which shows that $\langle n \rangle$, and therefore diffuse scattering intensity originating from phonons, will increase with temperature [3].

Figures S14 and S15 plot linecuts in \mathbf{Q} across several diffuse features from the XDS datasets of MAPbI₃ and MAPbBr₃ at different temperatures spanning the cubic to tetragonal structural transition. The top rows (a,b) show that the intensities of several X-points [(1.0, 0.5, 2.0), (2.0, 0.5, 2.0), (3.0, 0.5, 2.0), and (2.0, 2.0, 2.5)] remain constant or slightly increase with temperature. We attribute this behavior to standard phonon occupation statistics, demonstrating that the diffuse intensity at the X-point originates from energy-integrated inelastic scattering from phonons. The phonons at the X-points are explored in the following section and Fig. S16. Figs. S14c-f and S15c-f plot cuts along the R-point and across diffuse rods at the M-point respectively. Diffuse rods crossing the M-points are also visible in S14a,b and S15a,b. The intensity increases with decreasing temperature, in contrast with expected phonon behavior, with a sharp jump in intensity at the R-point indicating the transition to the tetragonal phase (for which the R-point is the Γ -point of the tetragonal Brillouin zone). The increase in intensity indicates an increase in the number and size of these tetragonal regions.

8 Phonons at the X- and R-points

The acoustic phonon dispersion along the Γ -X direction has been well studied in MAPbI₃ and MAPbBr₃ [14, 15] and is reproduced in our MD $S(\mathbf{Q}, E)$ calculations in Fig. S16 with both X-ray form-factors and neutron scattering lengths. These dispersions are also present in the INS $S(\mathbf{Q}, E)$ in Fig. S16d.

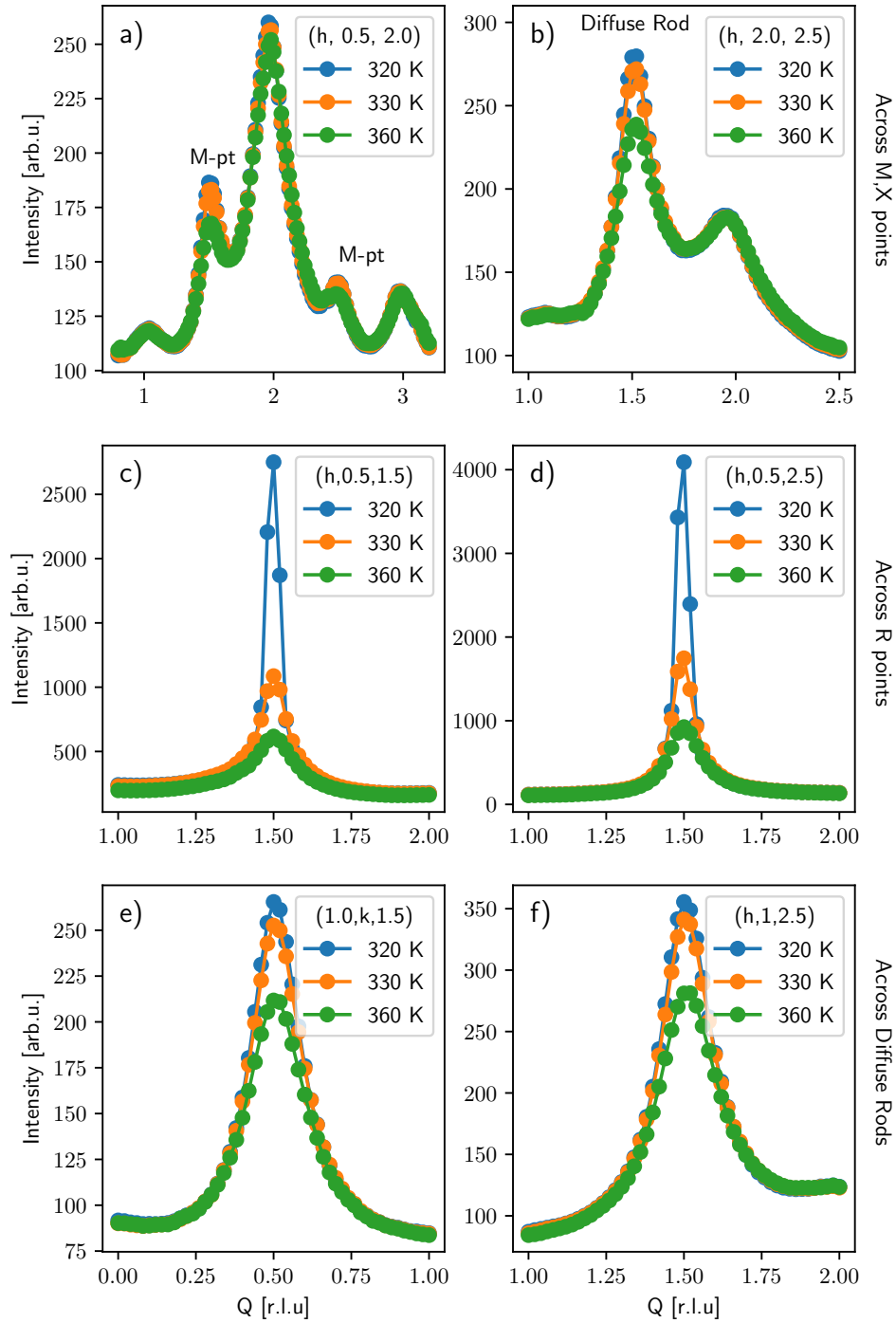


Fig. 14 Temperature dependence of the diffuse scattering in MAPbI₃ measured with XDS. At 330 and 360 K, MAPbI₃ is in the cubic $Pm\bar{3}m$ phase, whereas at 320 K MAPbI₃ is in the tetragonal $I4/mcm$ phase. In a), b), the cuts along h intercept X-points at full integer values and M-points (diffuse) rods at half integer values. In c), d) the R-point intensity shows a discontinuous jump across the cubic-tetragonal transition, whereas a more gradual increase in intensity with decreasing temperature is observed for the diffuse rods in e), f).

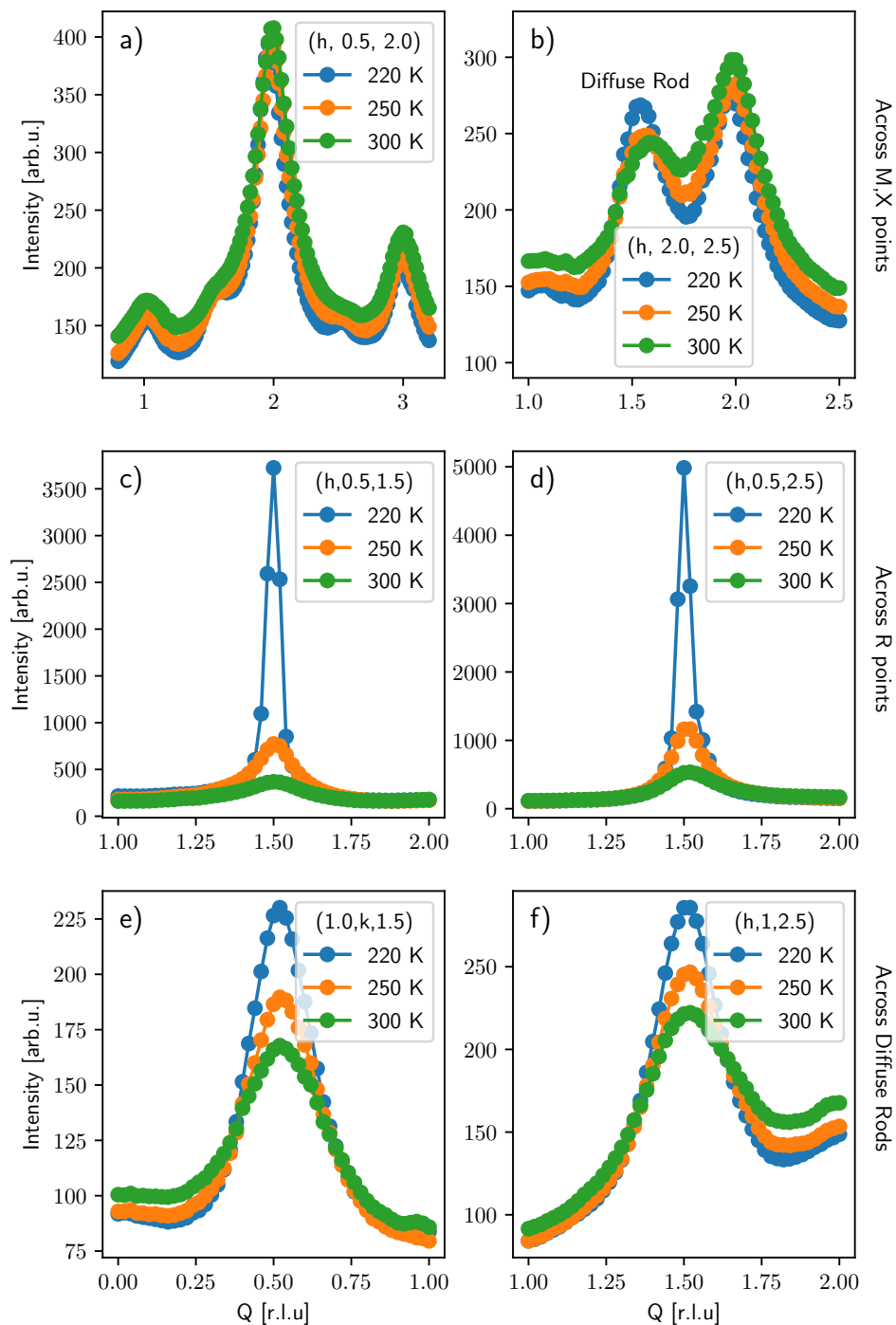


Fig. 15 Temperature dependence of the diffuse scattering in MAPbBr₃ measured with XDS. At 250 and 300 K, MAPbBr₃ is in the cubic $Pm\bar{3}m$ phase, whereas at 220 K MAPbBr₃ is in the tetragonal $I4/mcm$ phase. In a), b), the cuts along h intercept X-points at full integer values and M-points or diffuse rods at half integer values. In c), d) the R-point intensity shows a discontinuous jump across the cubic-tetragonal transition, whereas a more gradual increase in intensity with decreasing temperature is observed for the diffuse rods in e), f).

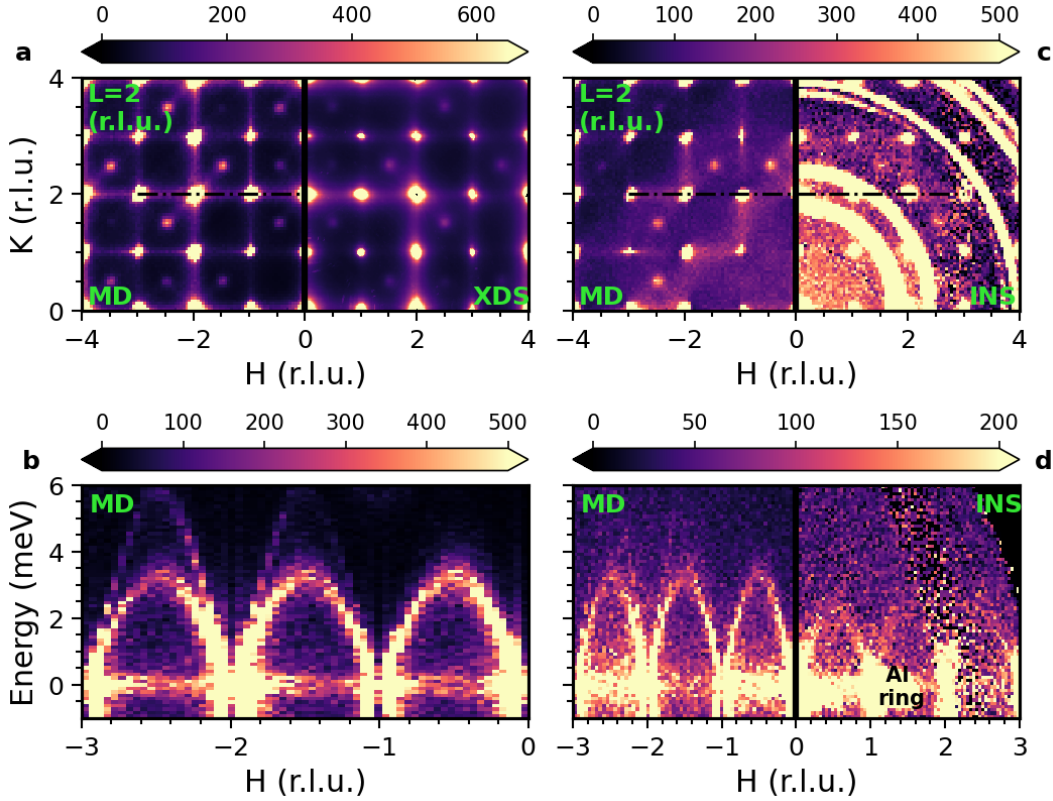


Fig. 16 a,c Diffuse scattering intensity in the L=2 plane from MD and experiment. a-b are x-rays and c-d are from neutrons. b and d show inelastic scattering from MD and experiment. Note, we do not have experimental inelastic x-ray data so the inelastic x-ray plot only contains theoretical results.

Given the low energy of these phonons, we expect them to contribute thermal diffuse intensity in both the XDS and NDS/INS experiments. In the $L = 2$ scattering plane, we indeed see rods of diffuse intensity along the Γ -X- Γ high symmetry direction. A careful inspection of the $S(\mathbf{Q}, E)$ in Fig. S16b and d show additional quasielastic intensity at $E = 0$. This intensity varies between BZs in the calculated neutron $S(\mathbf{Q}, E)$ in Fig. S16d, suggesting additional diffuse scattering contributions from the MA^+ cations.

Scattering is also observed at the X-point in the $L = 0.5, 1.5, 2.5$ planes in XDS and the energy-integrated MD $S(\mathbf{Q})$, but not NDS. This indicates an inelastic process with at least 0.5 meV energy transfer. X-ray and neutron spectroscopy have identified transverse and longitudinal acoustic phonons at the X-point with energies ranging from 2 - 5 meV in several hybrid LHPs [10, 14–17]. Therefore, it is likely that the broad diffuse intensity observed at the X-points originates from these phonons.

References

- [1] Van Hove, L.: Correlations in space and time and born approximation scattering in systems of interacting particles. *Physical Review* **95**(1), 249 (1954). <https://doi.org/10.1103/PhysRev.95.249>
- [2] Squires, G.L.: *Introduction to the Theory of Thermal Neutron Scattering*. Cambridge University Press, Cambridge, United Kingdom (2012). <https://doi.org/10.1017/CBO9781139107808>
- [3] Dove, M.T., Dove, M.T.: *Introduction to Lattice Dynamics*. Cambridge university press, Cambridge, United Kingdom (1993). <https://doi.org/10.1017/CBO9780511619885>
- [4] Harrelson, T.F., Dettmann, M., Scherer, C., Andrienko, D., Moulé, A.J., Faller, R.: Computing inelastic neutron scattering spectra from molecular dynamics trajectories. *Scientific reports* **11**(1), 1–12 (2021). <https://doi.org/10.1038/s41598-021-86771-5>
- [5] Hazemann, I., Dauvergne, M., Blakeley, M., Meilleur, F., Haertlein, M., Van Dorselaer, A., Mitschler, A., Myles, D.A., Podjarny, A.: High-resolution neutron protein crystallography with radically small crystal volumes: application of perdeuteration to human aldose reductase. *Acta Crystallographica Section D: Biological Crystallography* **61**(10), 1413–1417 (2005). <https://doi.org/10.1107/S0907444905024285>
- [6] Brown, P., Fox, A., Maslen, E., O’keefe, M., Willis, B.: Intensity of diffracted intensities. In: *International Tables for Crystallography vol. C*, pp. 554–595. Wiley Online Library, Hoboken, NJ, United States (2006). Chap. 6.1. <https://doi.org/10.1107/97809553602060000600>
- [7] Zushi, T., Ohmori, K., Yamada, K., Watanabe, T.: Effect of a SiO_2 layer on the thermal transport properties of $< 100 >$ Si nanowires: A molecular dynamics study. *Physical Review B* **91**(11), 115308 (2015). <https://doi.org/10.1103/PhysRevB.91.115308>
- [8] Xiong, S., Selli, D., Neogi, S., Donadio, D.: Native surface oxide turns alloyed silicon membranes into nanophononic metamaterials with ultralow thermal conductivity. *Physical Review B* **95**(18), 180301 (2017). <https://doi.org/10.1103/PhysRevB.95.180301>
- [9] Comin, R., Crawford, M.K., Said, A.H., Herron, N., Guise, W.E., Wang, X., Whitfield, P.S., Jain, A., Gong, X., McGaughey, A.J.H., Sargent, E.H.: Lattice dynamics and the nature of structural transitions in organolead halide perovskites. *Physical Review B* **94**(9), 094301 (2016). <https://doi.org/10.1103/PhysRevB.94.094301>

- [10] Beecher, A.N., Semonin, O.E., Skelton, J.M., Frost, J.M., Terban, M.W., Zhai, H., Alatas, A., Owen, J.S., Walsh, A., Billinge, S.J.L.: Direct Observation of Dynamic Symmetry Breaking above Room Temperature in Methylammonium Lead Iodide Perovskite. *ACS Energy Letters* **1**(4), 880–887 (2016). <https://doi.org/10.1021/acsenerylett.6b00381>
- [11] Weadock, N.J., Gehring, P.M., Gold-Parker, A., Smith, I.C., Karunadasa, H.I., Toney, M.F.: Test of the Dynamic-Domain and Critical Scattering Hypotheses in Cubic Methylammonium Lead Triiodide. *Physical Review Letters* **125**(7), 075701 (2020). <https://doi.org/10.1103/PhysRevLett.125.075701>
- [12] Mattoni, A., Filippetti, A., Saba, M., Delugas, P.: Methylammonium rotational dynamics in lead halide perovskite by classical molecular dynamics: the role of temperature. *The Journal of Physical Chemistry C* **119**(30), 17421–17428 (2015). <https://doi.org/10.1021/acs.jpcc.5b04283>
- [13] Allen, M.P., Tildesley, D.J.: *Computer Simulation of Liquids*. Oxford university press, ??? (2017)
- [14] Gold-Parker, A., Gehring, P.M., Skelton, J.M., Smith, I.C., Parshall, D., Frost, J.M., Karunadasa, H.I., Walsh, A., Toney, M.F.: Acoustic phonon lifetimes limit thermal transport in methylammonium lead iodide. *Proceedings of the National Academy of Sciences* **115**(47), 11905–11910 (2018). <https://doi.org/10.1073/pnas.1812227115>
- [15] Ferreira, A.C., Létoublon, A., Paofai, S., Raymond, S., Ecolivet, C., Rufflé, B., Cordier, S., Katan, C., Saidaminov, M.I., Zhumekenov, A.A., Bakr, O.M., Even, J., Bourges, P.: Elastic Softness of Hybrid Lead Halide Perovskites. *Physical Review Letters* **121**(8), 085502 (2018). <https://doi.org/10.1103/PhysRevLett.121.085502>
- [16] Songvilay, M., Giles-Donovan, N., Bari, M., Ye, Z.-G., Minns, J.L., Green, M.A., Xu, G., Gehring, P.M., Schmalzl, K., Ratcliff, W.D., Brown, C.M., Chernyshov, D., van Beek, W., Cochran, S., Stock, C.: Common acoustic phonon lifetimes in inorganic and hybrid lead halide perovskites. *Physical Review Materials* **3**(9), 093602 (2019). <https://doi.org/10.1103/PhysRevMaterials.3.093602>
- [17] Fujii, Y., Hoshino, S., Yamada, Y., Shirane, G.: Neutron-scattering study on phase transitions of CsPbCl₃. *Physical Review B* **9**(10), 4549–4559 (1974). <https://doi.org/10.1103/PhysRevB.9.4549>